

# A multilevel multimodal circuit enhances action selection in *Drosophila*

Tomoko Ohyama<sup>1\*</sup>, Casey M. Schneider-Mizell<sup>1\*</sup>, Richard D. Fetter<sup>1</sup>, Javier Valdes Aleman<sup>1</sup>, Romain Franconville<sup>1</sup>, Marta Rivera-Alba<sup>1</sup>, Brett D. Mensh<sup>1</sup>, Kristin M. Branson<sup>1</sup>, Julie H. Simpson<sup>1</sup>, James W. Truman<sup>1</sup>, Albert Cardona<sup>1</sup> & Marta Zlatic<sup>1</sup>

Natural events present multiple types of sensory cues, each detected by a specialized sensory modality. Combining information from several modalities is essential for the selection of appropriate actions. Key to understanding multimodal computations is determining the structural patterns of multimodal convergence and how these patterns contribute to behaviour. Modalities could converge early, late or at multiple levels in the sensory processing hierarchy. Here we show that combining mechanosensory and nociceptive cues synergistically enhances the selection of the fastest mode of escape locomotion in *Drosophila* larvae. In an electron microscopy volume that spans the entire insect nervous system, we reconstructed the multisensory circuit supporting the synergy, spanning multiple levels of the sensory processing hierarchy. The wiring diagram revealed a complex multilevel multimodal convergence architecture. Using behavioural and physiological studies, we identified functionally connected circuit nodes that trigger the fastest locomotor mode, and others that facilitate it, and we provide evidence that multiple levels of multimodal integration contribute to escape mode selection. We propose that the multilevel multimodal convergence architecture may be a general feature of multisensory circuits enabling complex input–output functions and selective tuning to ecologically relevant combinations of cues.

A single natural event, such as the attack of a predator, often presents multiple types of sensory cues, for example, visual, olfactory, tactile and noxious. These cues are detected separately by distinct sensors highly specialized for a single type of cue. Different sensory channels thus provide independent estimates of the same event that can be combined to improve sensitivity and reduce ambiguity<sup>1–3</sup>. Indeed, across the animal kingdom, multi-cue events often elicit enhanced reactions compared to single-cue stimuli<sup>1–5</sup>.

The enhancement in reactions to multi-cue stimuli is a result of convergence and integration of information from multiple modalities<sup>2,3,6</sup>. Because neurons can compute non-linear functions of their inputs, where convergence happens, and how often, determines the repertoire of input–output functions<sup>7</sup>. In artificial neural networks, a single layer of nonlinear units has strict restrictions in possible responses to combinations of inputs<sup>8,9</sup>. Adding a second layer that processes combinations of outputs from the first layer enables the network to implement far more complex input–output functions<sup>8–10</sup> and thus to discriminate far better between different combinations of inputs. Similarly, in the nervous system, an architecture in which neurons that receive different combinations of inputs from two modalities in one level converge on neurons in downstream levels could enable better discrimination between different kinds of multimodal stimuli and selective tuning to specific ecologically relevant combinations of the two cues.

The structural and functional architecture of multisensory convergence across multiple levels of the sensory processing hierarchy is an open question for any large nervous system. Neurons that integrate information from multiple modalities have been most extensively studied in higher-order and motor-control areas<sup>2,3,6,11–17</sup>. Multi sensory interactions have also been described at earlier stages of sensory processing<sup>3,18–21</sup>. However, it is unclear whether the multisensory

neurons observed at distinct levels are structurally or functionally connected, and whether they contribute to the same behaviour.

The *Drosophila* larva is an excellent model system to study the structural and functional patterns of multimodal interactions across multiple levels of the sensory processing hierarchy and how these patterns contribute to behaviour. The relatively small size of its 10,000-neuron nervous system makes it amenable to circuit mapping using large scale electron microscopy reconstruction<sup>22,23</sup>. Powerful genetic tools enable functional studies of uniquely identifiable neurons<sup>24–26</sup>.

Larvae have distinct sensory modalities with which they can gauge the degree of threat<sup>27–31</sup> and an array of distinct escape behaviours available for responding to threats, such as turning, digging, fast crawling and rolling<sup>27,28,31–35</sup>. The most vigorous escape sequence consists of two locomotion modes: rolling followed by fast crawling<sup>28,32</sup>. Rolling is the fastest—and presumably the most energetically costly<sup>27,28</sup>. A range of distinct aversive cues can evoke the fast crawling response without rolling, including mild nociceptive and strong mechanosensory stimulation<sup>28,35</sup>. In contrast, rolling is observed in extremely threatening situations, such as strong noxious stimulation<sup>27,28,32,33,36</sup>, or predator attack<sup>27,32</sup>, the latter of which provides multiple cues, including nociceptive and mechanosensory<sup>27,31,32</sup>.

Here we show that mechanosensory combined with nociceptive cues synergistically increase the likelihood of rolling, and use this tractable model system to determine the anatomical and functional patterns of convergence supporting the synergy.

## Multisensory cues enhance the selection of rolling

We developed an automated multisensory assay in which we activate larval nociceptive multidendritic class IV (MD IV) neurons thermogenetically<sup>32,36</sup> and larval mechanosensory chordotonal neurons using vibration<sup>28,31</sup> (Fig. 1a, b and Extended Data Fig. 1a–d).

<sup>1</sup>Howard Hughes Medical Institute Janelia Research Campus, 19700 Helix Drive, Ashburn, Virginia 20147, USA.

\*These authors contributed equally to this work.

§These authors jointly supervised this work.

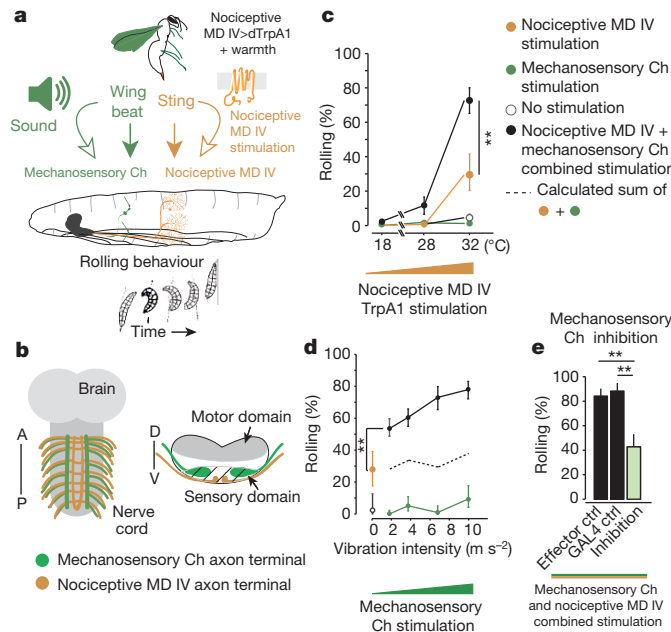


**Figure 1 | Mechanical and nociceptive stimulation synergistically trigger rolling.** **a**, Schematic of a high-throughput multisensory assay for presenting stimuli similar to wasp attack. Speaker-emitted vibration (green) sensed by chordotonal (Ch) neurons replaces the mechanosensory stimulus. Thermogenetic activation of MD IV neurons (orange) using the transgenic temperature-sensitive channel, dTRPA1, and exposing *MD IV-GAL4>UAS-dTrpA1* larvae to warmth (30 °C or 32 °C), replaces the noxious sting. **b**, Chordotonal and MD IV neurons from each hemisegment project to distinct modality-specific ventrolateral and ventromedial regions of the nerve cord, respectively. A, anterior; P, posterior; D, dorsal; V, ventral. See Supplementary Table 1 for *n* (animals) in this and all other figures. See Supplementary Table 2 for a list of genotypes used in this and all other figures. **c, d**, Percentage of animals that rolled in response to mechanical (green, *MD IV-GAL4/+*), nociceptive (orange, *MD IV-GAL4>UAS-dTrpA1*), combined (black, *MD IV-GAL4>UAS-dTrpA1*), or no (white, *MD IV-GAL4/+*) stimulation, when either MD IV activation is increased, given constant vibration (1,000 Hz, 6.7 m s<sup>-2</sup>; **c**), or vibration is increased, given constant nociceptor activation (32 °C; **d**). Error bars, 95% confidence interval; \*\**P* < 0.0001,  $\chi^2$  test with Holm-Bonferroni correction. **e**, Hyperpolarizing chordotonal neurons reduced rolling in response to bimodal mechanical and nociceptive stimulation (32 °C and 1,000 Hz, 6.7 m s<sup>-2</sup> in this and subsequent figures) using the transgenic inward rectifying potassium channel Kir in *MD IV-LexA>lexAop-dTRPA1, ch-GAL4>UAS-Kir* animals. Ctrl, controls.

Different combinations of nociceptive and mechanosensory stimulation induced different likelihoods of the key escape sequences: rolling followed by fast crawling versus fast crawling alone. Nociceptor activation alone evoked a relatively low likelihood of rolling (Fig. 1c, d, Extended Data Fig. 1e and Supplementary Video 1) and a high likelihood of fast crawling<sup>28</sup> (Extended Data Fig. 1e, f). Vibration alone evoked only fast crawling<sup>28,33</sup> (Extended Data Fig. 1e, f) and essentially no rolling (Fig. 1c, d and Supplementary Video 2).

Combined with nociceptor activation, vibration increased the likelihood of rolling; the effect is dose-dependent and super-additive (synergistic) (Fig. 1c, d, Extended Data Fig. 1g and Supplementary Video 3). This vibration-induced facilitation of rolling was mediated through the mechanosensory chordotonal neurons (Fig. 1e).

## First-order multisensory interneurons trigger rolling

We suspected that the information from the two modalities converges onto central neurons involved in the selection of rolling. To identify such neurons and thus determine where in the sensory processing hierarchy multisensory convergence occurs, we performed a behavioural screen for neurons whose thermogenetic activation triggers rolling (see Methods). We identified a 'hit', the *R72F11* *Drosophila*

line, that drove GAL4 expression in neurons potentially early in the sensory processing hierarchy (Fig. 2a–c and Extended Data Fig. 2a, b). Activating the neurons in *R72F11* triggered rolling in a significant fraction of animals (Fig. 2a and Supplementary Videos 4 and 5), and inhibiting them (see Methods) significantly decreased rolling in response to bimodal stimulation (Fig. 2b).

*R72F11* drives expression selectively in four lineage-related, segmentally repeated projection neurons with basin-shaped arbors in the ventral, sensory domain of the nerve cord; we therefore named them Basins-1–4 (Fig. 2c, d and Extended Data Fig. 2a–c). The dendrites of Basin-1 and Basin-3 span a ventrolateral domain of the nerve cord, where the mechanosensory chordotonal terminals are located<sup>37,38</sup> (Fig. 2c, d and Extended Data Fig. 2c, d). The dendrites of Basin-2 and Basin-4 span both the ventrolateral chordotonal domain and a ventromedial domain where the nociceptive MD IV terminals are located<sup>37–39</sup> (Fig. 2c, d and Extended Data Fig. 2c, d). We therefore asked whether the mechanosensory chordotonal and the nociceptive MD IV neurons directly converge on Basin-2 and Basin-4.

In an electron microscopy volume that spans 1.5 nerve cord segments, we reconstructed the chordotonal and MD IV arbors (Fig. 2e and Extended Data Fig. 2e, f) and all of their synaptic partners (a total of 301 neuronal arbors) (Fig. 2e, Extended Data Fig. 3a–d and Supplementary Table 4a–c). Amongst the reconstructed neurons we recognized the left and right Basin-1, -2, -3 and -4 homologues (Fig. 2d, f and Extended Data Fig. 2c, d, g, h).

Basin-1 and Basin-3 received many inputs (each >25 synapses and >15% of total input, on average) from chordotonal neurons, but very few (no more than 1% of total input synapses) from MD IV neurons (Fig. 2g and Extended Data Fig. 2i, j). Basin-2 and Basin-4 received many inputs from both chordotonal neurons (on average >20 synapses and >10% total input) and MD IV neurons (on average >20 synapses and >10% total input) (Fig. 2g and Extended Data Fig. 2i, j), each on distinct dendritic branches (Fig. 2h). Of all the 301 partners downstream of MD IV and chordotonal neurons, only Basin-2 and Basin-4 reproducibly received >5 synapses from both chordotonal and MD IV neurons (Fig. 2i), suggesting that they are probably key integrators of chordotonal and MD IV inputs.

To investigate whether the observed anatomical inputs from the sensory neurons onto Basins were functional and excitatory, we imaged calcium transients in response to MD IV or chordotonal activation (see Methods) collectively in all Basins (Extended Data Fig. 4a–d) or in individual Basin types (Fig. 3a, b), using lines that drive expression selectively in Basin-1 or Basin-4 neurons (Extended Data Fig. 4e–h).

In Basin-1, we observed calcium transients in response to vibration, but not in response to MD IV activation (Fig. 3a), consistent with the large number of synapses it receives from chordotonal neurons and the relatively few from MD IV neurons (Fig. 2g and Extended Data Fig. 2i). In Basin-4, we observed calcium transients in response to both vibration and MD IV activation (Fig. 3b), consistent with the large number of synapses it receives from both sensory types (Fig. 2g and Extended Data Fig. 2i). Basin-4 integrated the inputs from the two modalities, responding significantly more to bimodal than to unimodal stimulation (Fig. 3b, c and control in Extended Data Fig. 4i, j).

Next, we asked whether the multisensory Basin-4 interneurons contribute to rolling selection. Silencing Basin-4 neurons significantly decreased rolling in response to bimodal stimulation, indicating these neurons are involved in triggering rolling (Fig. 3d). Selective activation of the multisensory Basin-4 interneurons triggered rolling in a dose-dependent way, with strongest activation triggering rolling in 45% of animals (Fig. 3e).

We also wondered whether a second level of multimodal integration (that is, integration of information from distinct Basin types, that receive distinct combinations of chordotonal and MD IV inputs), enhances the selection of rolling. Indeed, co-activation of Basin-1 with the bimodal Basin-4 facilitated rolling (Fig. 3e), resulting in a

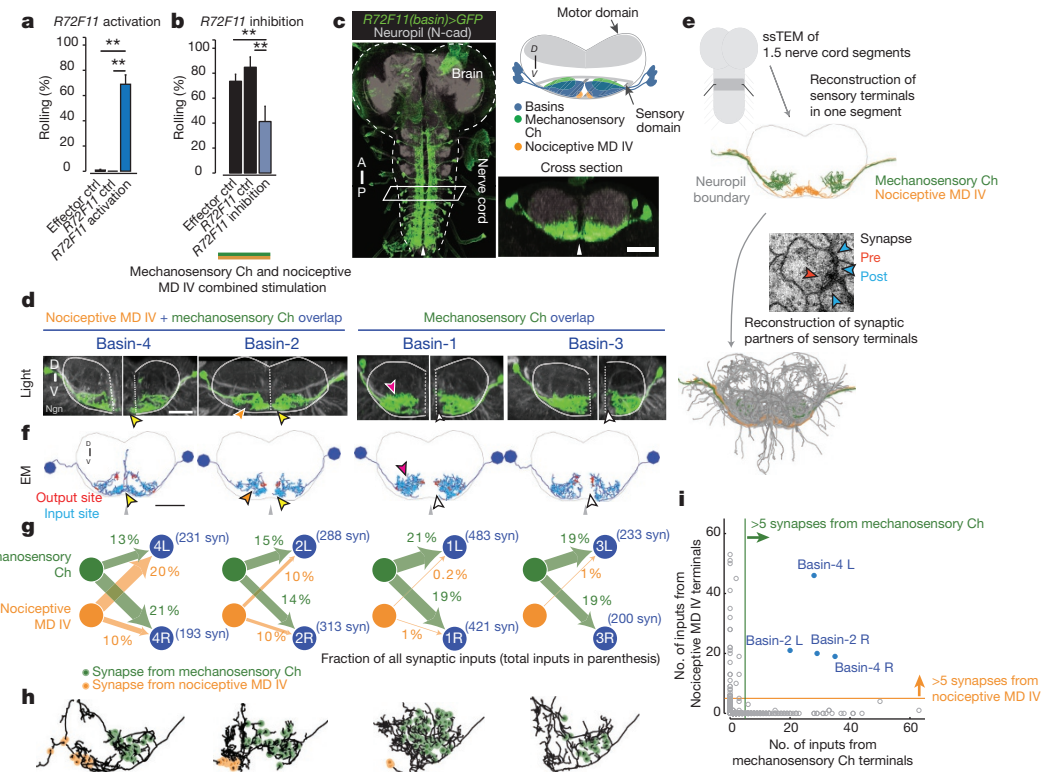


**Figure 2 | Activation screen and electron microscopy reconstruction reveal first-order multisensory interneurons.** **a**, Thermogenetic activation of neurons in *R72F11* (exposing *R72F11-GAL4>UAS-dTrpA1* larvae to 32 °C) triggered rolling. Error bars, 95% confidence interval; \*\* $P < 0.0001$ ,  $\chi^2$  test with Holm-Bonferroni correction. **b**, Silencing neurons in *R72F11* significantly reduced rolling in response to bimodal stimulation (in *MD IV-LexA>lexAop-dTRPA1, R72F11-GAL4>UAS-Kir* animals). Ch, chordotonal. **c**, *R72F11* drives expression in Basin neurons (green, *R72F11-GAL4>UAS-GFP*). Scale bar, 25  $\mu$ m. Arrowheads indicate midline. **d**, Four Basin types visualized with a FLP-based strategy are identifiable based on unique combinations of dendritic features: medial projection (yellow arrowhead); ventrolateral indentation (orange arrowhead); bushy dorsal arbor (red arrowhead); and absence of medial projection (white arrowhead). Solid white outlines, neuropil boundary;

significantly higher likelihood of rolling compared to activation of Basin-4 alone (70% versus 45%). Thus, information from distinct Basin types may converge again onto downstream neurons involved in triggering rolling.

### Goro neurons in motor nerve cord trigger rolling

To identify potential sites of convergence of information from the different types of first-order Basin interneurons we looked at a ‘hit’ from the thermogenetic activation screen, *R69F06*, a *Drosophila* line that drove GAL4 expression in neurons that project far from the early sensory processing centres (Fig. 4a–c). Thermogenetic activation of neurons in *R69F06* triggered rolling in a high fraction of larvae (Fig. 4a and Supplementary Video 6), and inhibiting them significantly decreased rolling in response to bimodal stimulation (Fig. 4b).

*R69F06* drives expression in a few neurons in the brain, in the suboesophageal zone (SEZ) and in a pair of thoracic neurons whose axons descend through the dorsal, motor domain of the nerve cord (Fig. 4c–e). Selectively activating the single pair of thoracic neurons (see Methods and Extended Data Fig. 5a–d) triggered rolling in 76% of larvae (Fig. 4e, f). We named these command-like neurons Goro (a romanization of the Japanese for rolling).

Activation of Basins evoked strong calcium transients in the Goro neurons, indicating that these cell types involved in the same behaviour are functionally connected (Fig. 4g, h and Extended Data Fig. 5e, f). To identify the shortest anatomical pathways from Basins to Goro that

dashed lines, midline. Neuropil is visualised with labelling against N-cadherin (N-cad) in **c** or neuroglial (Ngn) in **d**. Scale bar, 20  $\mu$ m. **e**, Electron microscopy reconstruction of all direct synaptic targets of the chordotonal (eight left and eight right) and MD IV (three left and three right) neurons in the abdominal segment A3. ssTEM, serial section transmission electron microscopy.

**f**, Amongst the reconstructed arbor, we recognized Basins, based on morphological features (arrowheads). Grey arrow, midline. Scale bar, 10  $\mu$ m. **g**, The fraction of inputs onto Basins originating from chordotonal or MD IV terminals. **h**, Synaptic inputs from MD IV (orange circles) and chordotonal (green circles) segregate onto distinct dendritic branches of Basin-2 and Basin-4. **i**, Plot shows the number of synapses from chordotonal and MD IV terminals onto each of the 301 downstream partners. L, Basin homologue from the left hemisegment; R, Basin homologue from the right hemisegment.

might support the observed functional connectivity and to determine whether the information from distinct Basin types converges onto Goro, we again used electron microscopy reconstruction.

### Nerve cord and brain pathways from Basins to Goro

We used a second electron microscopy volume (from a second larva) that spans the entire larval nervous system and therefore also includes Goro neurons (Fig. 5a and Supplementary Video 7). In the new volume, we reconstructed chordotonal, MD IV and Basin neurons from segment A1, as well as the Goro neurons (Fig. 5a–c, Extended Data Figs 2g–j and 3a–d, Supplementary Table 5a–c and Supplementary Video 8).

To find putative pathways from distinct Basin types to Goro neurons, we first reconstructed all neurons downstream of all axonal outputs from the four left and right Basin homologues from segment A1 (Fig. 5d, e, Supplementary Information (Supplementary Atlas section) and Supplementary Tables 5 and 6). We identified 31 pairs of reproducible downstream partners (Fig. 5d, e and Supplementary Information (Supplementary Atlas section)). Amongst these we identified second-order nerve cord interneurons that constitute the shortest pathways from Basins to Goro neurons (called A05q and A23g where ‘A’ stands for abdominal neuron; Fig. 5d). They receive inputs from distinct Basin types and synapse onto Goro neurons (Fig. 5d). Thus, information from distinct Basin types, that receive distinct combinations of MD IV and chordotonal inputs, converges onto Goro neurons—providing a second level of multimodal convergence.

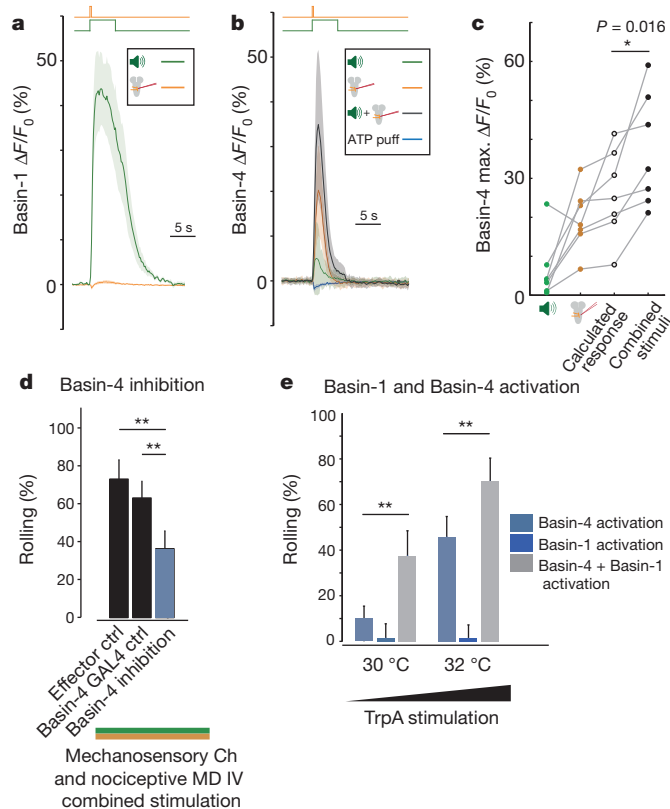


**Figure 3 | Multiple levels of multimodal integration.** **a**, Calcium transients (mean  $\pm$  s.e.m.) are evoked in Basin-1 dendrites by vibration (1,000 Hz,  $6.7 \text{ ms}^{-2}$ , 5 s, symbolized by green speaker; green trace;  $n = 7$  trials), but not by MD IV activation with transgenic ATP-gated channel, P2X<sub>2</sub>, and local injection of ATP (symbolized by orange injection electrode; orange trace;  $n = 6$  trials; *MD IV-lexA>laxAop-P2X<sub>2</sub>*; *Basin-1-GAL4>UAS-GCaMP6*). **b**, Calcium transients (mean  $\pm$  s.e.m.) are evoked in Basin-4 dendrites by vibration (green trace), nociception (orange trace) and combined stimulation (black trace;  $n = 7$  triplet trials; *MD IV>P2X<sub>2</sub>*; *Basin-4>GCaMP6*); but not by ATP injection in the absence of P2X<sub>2</sub> expression (blue trace, *MD IV>+*; *Basin-4>GCaMP6*). **c**, Peak  $\Delta F/F_0$  from **e** shows Basin-4 response to combined stimulation (filled black circles) is significantly higher (paired  $t$ -test) than the calculated sum of unisensory responses (clear black circles). **d**, Silencing Basin-4 neurons significantly reduced rolling evoked by bimodal stimulation (in *MD IV-LexA>laxAop-dTRPA1*, *Basin-4-GAL4>UAS-Kir* animals) compared to controls. Ch, chordotonal. **e**, Thermogenetic activation of Basin-4 neurons evoked rolling (exposing *Basin-4-GAL4>UAS-dTrpA1* animals to 30 °C or to 32 °C). Basin-1 facilitated rolling in combination with Basin-4 (exposing *Basin-4-GAL4*, *Basin-1-GAL4>UAS-dTrpA1* animals to 30 °C or to 32 °C). Error bars, 95% confidence interval; \*\* $P < 0.0001$ ,  $\chi^2$  test with Holm–Bonferroni correction.

Ten distinct second-order projection neuron types downstream of Basins ascend to the brain (Fig. 5e and Supplementary Information (Supplementary Atlas section)). Some of these integrate Basin information across multiple distal segments of the body, either exclusively from a single Basin type (for example, A00c-a6, Fig. 5e), or from distinct Basin types (that receive distinct combinations of sensory inputs; for example, A00c-a4 and A00c-a5, Fig. 5e). Then, distinct second-order PNs, that receive distinct combinations of Basin inputs (and therefore distinct combinations of mechanosensory and nociceptive inputs), re-converge again on third-order interneurons in the brain (Fig. 5f). Thus, following convergence of local mechanosensory and nociceptive information from a single segment onto multisensory Basins, global mechanosensory and multisensory information from multiple segments is integrated within the brain pathway.

By tracing upstream of Goro dendritic inputs (Fig. 5f and Supplementary Atlas) we identified brain neurons which send

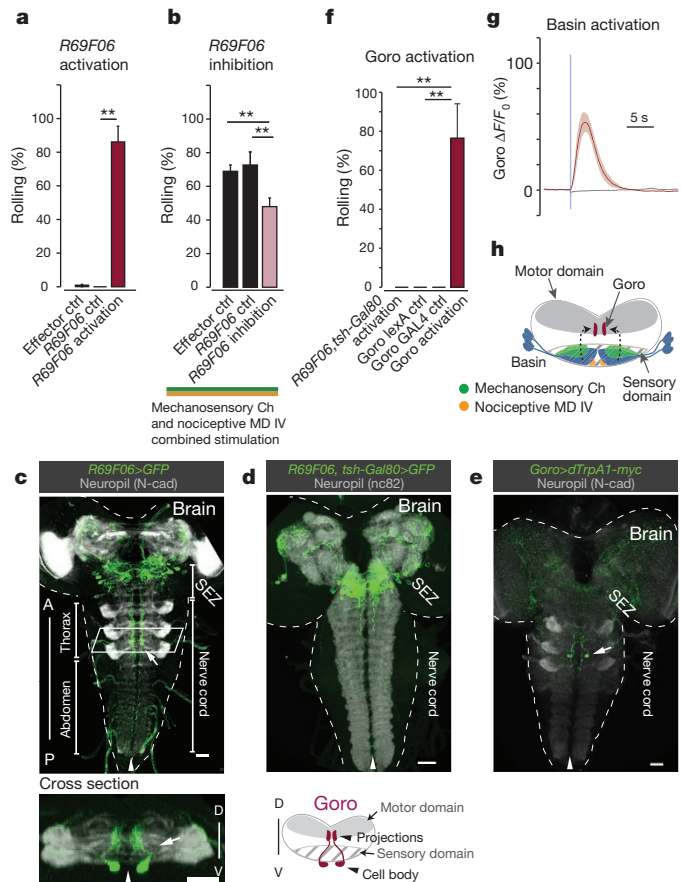


**Figure 4 | Basins are functionally connected to command-like Goro neurons.** **a**, Thermogenetic activation of neurons in *R69F06* triggered rolling (exposing *R69F06-GAL4>UAS-dTrpA1* to 32 °C). **b**, Silencing neurons in *R69F06* significantly reduced rolling in response to bimodal stimulation (*MD IV-LexA>laxAop-dTRPA1*, *R69F06-GAL4>UAS-Kir*). Ch, chordotonal. **c–e**, Images of neurons (green) in *R69F06>GFP* (**c**), *R69F06, tsh-Gal80>GFP* (**d**) and *Goro>dTRPA1-myc* (*R16F11-LexA>laxAop-FLP*, *R69F06-GAL4>UAS-FRT-STOP-FRT-dTRPA1-myc* (**e**) animals. Scale bar, 25  $\mu\text{m}$ . Arrowheads indicate midline. **f**, Thermogenetic activation of the single pair of Goro neurons triggered rolling in 76% of animals (exposing *Goro>dTRPA1-myc* from the *R16F11-LexA>laxAop-FLP*, *R69F06-GAL4>UAS-FRT-STOP-FRT-dTRPA1-myc* cross to 32 °C); thermogenetic activation of only the brain and SEZ neurons in *R69F06* did not (exposing *R69F06, tsh-Gal80>dTRPA1* to 32 °C). Error bars, 95% confidence interval; \*\* $P < 0.0001$ ,  $\chi^2$  test with Holm–Bonferroni correction. **g**, Basin activation by local ATP injection (in *72F11>P2X<sub>2</sub>*, *R69F06>GCaMP* animals) evoked calcium transients (mean  $\pm$  s.e.m.) in Goro dendrites (red trace,  $n = 9$  trials); ATP injection in the absence of P2X<sub>2</sub> (in *72F11>+*; *R69F06>GCaMP* animals) did not (grey trace,  $n = 8$  trials). **h**, Summary of the identified functional pathway involved in triggering rolling.

descending axons that synapse onto Goro neurons. Tracing downstream of a multisensory second-order ascending projection neuron (A00c-a4), we identified third-order projection neurons connecting the ascending pathways from Basins to a descending path onto Goro neurons (Fig. 5f). Thus, the activity of the command-like Goro neurons may be modulated by the more local multisensory and unisensory information via the nerve cord Basin–Goro pathway and by the global body-wide nociceptive and mechanosensory multisensory information via the brain Basin–Goro pathways (Fig. 5d–f).

We also identified a third-order SEZ feedback neuron that receives convergent body-wide mechanosensory and multisensory information and descends through the nerve cord sensory domain (Fig. 5g). The SEZ feedback neuron synapses onto the first-order (Basins) and second-order neurons from both the nerve cord (A05q) and brain (A00c) Basin–Goro pathways (Fig. 5g). Both the nerve cord and brain

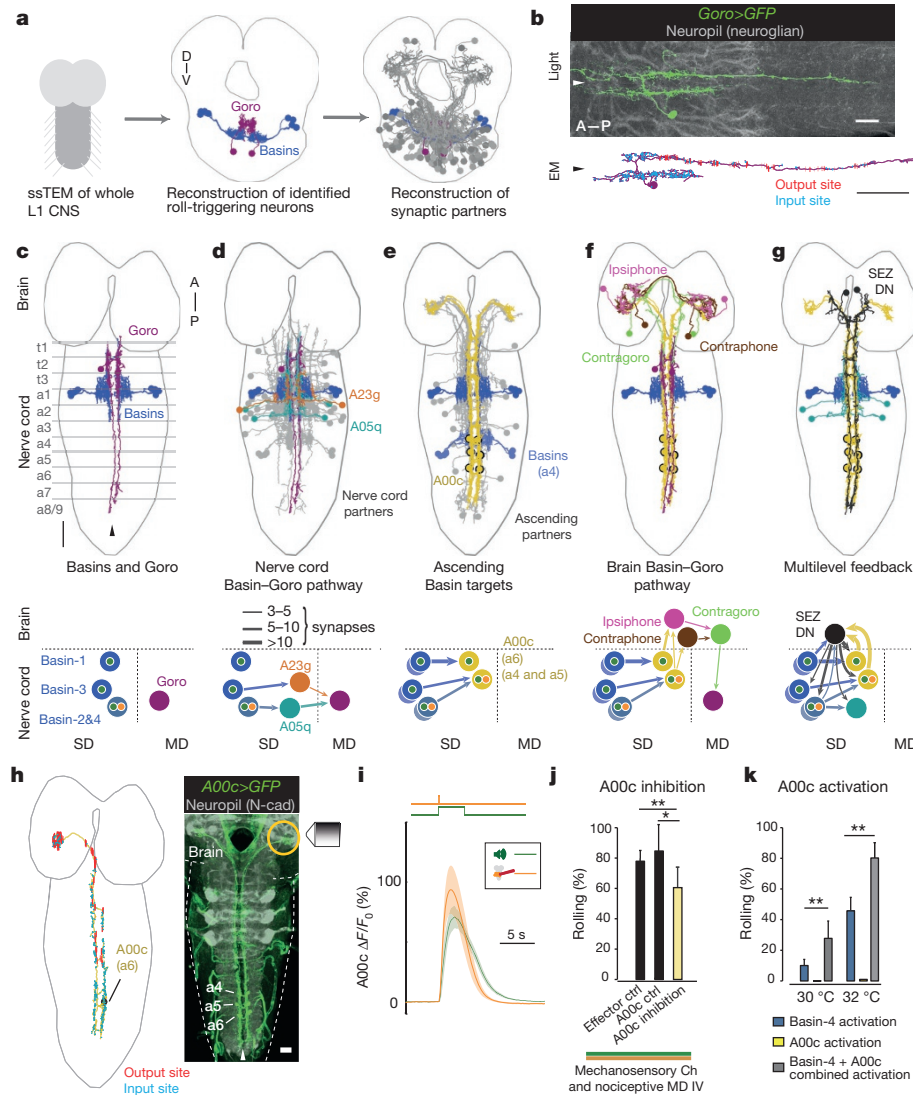


**Figure 5 | Electron microscopy reconstruction reveals multiple levels of multimodal convergence within Basins-to-Goro pathways.**

**a**, Electron microscopy reconstruction of the Basin–Goro anatomical pathways. ssTEM, serial section transmission electron microscopy.

**b**, Confocal image (green) and electron microscopy (EM) reconstruction of a single Goro neuron (magenta; see also Supplementary Video 8). Arrowheads indicate midline. Scale bars, 20  $\mu\text{m}$ . **c–h**, Reconstructed interneurons (top) and their connectivity (bottom). MD, motor domain; SD, sensory domain. **c**, Reconstructed Basins and Goro neurons. **d**, Mechanosensory Basin target A23g and multisensory Basin target A05q converge onto Goro neurons. Grey, all other Basin targets that project to the nerve cord. **e**, Distinct A00c (yellow) ascending projection neurons integrate information from distinct combinations of Basins across multiple segments. Grey, all other Basin targets that ascend to the brain. **f**, Third-order brain projection neurons, ipsiphone and contraphone, receive inputs from the A00c neurons and synapse onto brain neurons (contragoro) that send descending axons into the nerve cord and synapse onto Goro. **g**, Feedback neurons from SEZ. DN, descending neuron.

**h**, Electron microscopy reconstruction of a single A00c-a6 neuron and confocal image of all three pairs of A00c-a4/a5/a6 neurons in line R71A10. **i**, Calcium transients (mean  $\pm$  s.e.m.) in the terminals of all A00c cells (in MD IV> $P2X_2$ , R71A10> $GCaMP$  animals) shows they respond to MD IV activation by local ATP injection (orange trace,  $n = 12$  trials) and vibration (green trace,  $n = 4$  trials). **j**, Silencing A00c neurons significantly reduces rolling in response to bimodal stimulation (in MD IV-LexA> $lexAop-dTRPA1$ , R71A10-GAL4> $UAS-Kir$  animals). Ch, chordotonal. **k**, A00c neurons facilitate rolling in combination with Basin-4 (exposing Basin-4-GAL4, R71A10-GAL4> $UAS-dTrpA1$  animals to 30 °C or to 32 °C). Error bars, 95% confidence interval; \*\* $P < 0.0001$ ,  $\chi^2$  test with Holm–Bonferroni correction.

Basin–Goro pathways may therefore be jointly regulated based on integrated global multisensory information.

### Function of distinct pathways in triggering rolling

Next we wanted to explore the functional role of the nerve cord and brain Basin–Goro pathways. Basin activation could activate Goro neurons in the absence of the brain, suggesting the nerve cord Basin–Goro pathway is excitatory and sufficient for activating Goro neurons and triggering rolling (Extended Data Fig. 6a, b). Consistent with this idea, Basin activation evoked calcium transients in their nerve-cord targets, the A05q neurons, and A05q activation evoked calcium transients in Goro neurons, (Extended Data Fig. 6c–g). Furthermore, thermogenetic activation of the neurons in a line that drives expression, amongst others, in the A05q neurons triggered rolling (Extended Data Fig. 6c, h).

Calcium imaging in the terminals of three Basin-target neurons that ascend to the brain (A00c-a6, A00c-a5 and A00c-a4) (Fig. 5h) revealed that, collectively, they respond to vibration, to MD IV activation, and to Basin activation, suggesting that this connection is also excitatory (Fig. 5i and Extended Data Fig. 6i, j).

Silencing the A00c neurons decreased rolling in response to bimodal stimulation (Fig. 5j), and their co-activation with Basin-4 facilitated rolling (Fig. 5k). Therefore, downstream from early local

multisensory integration by Basin-4, additional levels of integration of global mechanosensory and multisensory information appear to further facilitate the transition to rolling behaviour.

### Differential effects on triggering roll and crawl

The rolling response triggered by multisensory cues (or by strong nociceptive cues alone) is followed by fast crawling<sup>28</sup> (Extended Data Fig. 1e, f). Similarly, optogenetic<sup>40</sup> activation of the first-order multisensory Basin-4 neurons triggered both locomotor modes; rolling followed by fast crawling (Extended Data Fig. 7a–c). However, optogenetic activation of the Goro neurons triggered only rolling, but not fast crawling, suggesting that they act as dedicated command-like neurons for rolling (Extended Data Fig. 7a–c). This also suggests that the act of rolling itself is insufficient to trigger fast crawling. In the future it will be interesting to determine how all of the 31 novel neuron types directly downstream of the Basins identified in our electron microscopy reconstruction (Supplementary Information (Supplementary Atlas section)) contribute to the selection of the two locomotor modes, rolling and crawling, in a defined sequence.

### Discussion

By combining behavioural and physiological studies with large-scale electron microscopy reconstruction we mapped a multisensory circuit

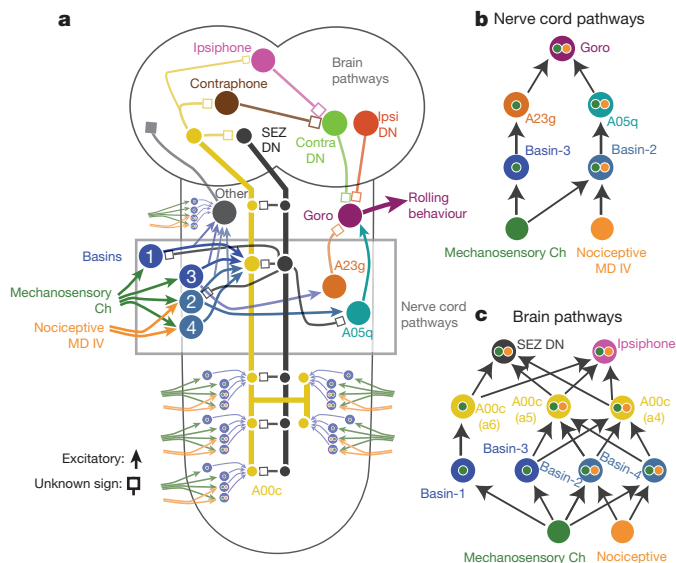


**Figure 6 | Summary of the multilevel multimodal convergence circuit for rolling.** **a**, Whole-animal circuit. Ch, chordotonal. **b, c**, Specific nerve cord (**b**) and brain (**c**) pathways Arrow, excitatory connections. Square, connections of unknown sign.

that mediates the selection of the fastest mode of escape locomotion (rolling) in *Drosophila* larva (Fig. 6a, b). We find that mechanosensory and nociceptive sensory neurons converge on specific types of first-order multisensory interneurons that integrate their inputs. Then, interneurons that receive distinct combinations of mechanosensory and nociceptive inputs converge again at multiple levels downstream, all the way to command-like neurons in the nerve cord. Activating just a single type of first-order multisensory interneuron triggers rolling probabilistically. Co-activation of first-order interneurons that receive distinct combinations of mechanosensory and nociceptive inputs increases rolling probability. Thus, action selection starts at the first-order multisensory interneurons and multiple stages of multimodal integration in the distributed network enhance this selection.

Given that spurious firing from distinct sensors is uncorrelated, whereas event-derived signals will be temporally correlated across the sensory channels, multimodal integration even at a single level improves the signal-to-noise ratio<sup>1,3,41</sup>. Multilevel multimodal integration can offer additional advantages. Theoretical studies show that a multilevel convergence architecture enables more complex input-output relationships<sup>7–10</sup>. Similarly, the multilevel multimodal convergence architecture described here could offer better discrimination between different kinds of multisensory events. The weights in such networks could be tuned either through experience or through evolution to respond selectively to highly specific combinations of two cues. Using a simple model, we can demonstrate (Extended Data Fig. 8a–k) that compared to early-convergence a multilevel architecture could specifically enhance the selection of the fastest escape mode in the most threatening situations, either in response to weak multimodal or strong unimodal nociceptive cues.

The multilevel multimodal convergence architecture may be a general feature in multisensory integration circuits, enabling complex response profiles tunable to specific ecological needs. For example, physiological studies in mammals have identified multisensory neurons that integrate the same cues at several stages in the sensory processing hierarchy<sup>18,19,21,42,43</sup>, although it is unclear whether the multisensory neurons at distinct levels are causally related to the same behaviour. Due to the size of networks involved, synaptic-level resolution studies of the underlying convergence architecture across multiple levels were unattainable.

In addition to the multilevel multimodal feed-forward convergence motif, our electron microscopy reconstruction revealed higher-order and local feedback neurons (Figs 5g and 6a and Supplementary Information (Supplementary Atlas section)). Recent theoretical models of multisensory integration suggest that the output of individual multisensory neurons is normalized by the activity of other multisensory neurons in that population, but the anatomical implementation of such feedback has not been identified<sup>2,44</sup>. Some of the feedback neurons in the multisensory circuit described in this study may have roles in such normalization computations.

Another circuit motif revealed by our study is the divergence of sensory information into nerve cord and ascending brain pathways and subsequent re-convergence of the shorter and the longer pathway onto the same command-like neurons in motor nerve cord (Goro). The nerve cord pathway integrates nociceptive and mechanosensory information from a local region of the body (few segments), whereas the ascending brain pathway integrates the information across all body segments and provides a means of modulating command-like neuron activity based on global body-wide nociceptive and mechanosensory information. The multisensory circuit described here in a genetically tractable model system provides a resource for investigating in detail how multiple brain and nerve cord pathways interact with each other and contribute to the selection of different modes of locomotion (rolling and crawling) in a defined sequence.

The electron microscopy volume spanning the entire insect nervous system acquired for this study can be used to map circuits that mediate many different behaviours. Combining information from a complete wiring diagram with functional studies has been very fruitful in the 302-neuron nervous system of *C. elegans*<sup>45,46</sup>. Recently, similar approaches have been applied to microcircuits in smaller regions of larger nervous systems<sup>47–50</sup>. In this manuscript, we demonstrate that relating local and global structure to function in a complete nervous system is now possible for the larger and more elaborate nervous system of an insect.

**Online Content** Methods, along with any additional Extended Data display items and Source Data, are available in the online version of the paper; references unique to these sections appear only in the online paper.

Received 5 August 2014; accepted 6 February 2015.

Published online 20 April 2015.

- Stein, E. B. & Meredith, M. A. *The Merging of the Senses* (MIT press, 1993).
- Fetsch, C. R., DeAngelis, G. C. & Angelaki, D. E. Bridging the gap between theories of sensory cue integration and the physiology of multisensory neurons. *Nature Rev. Neurosci.* **14**, 429–442 (2013).
- van Aerteldt, N., Murray, M. M., Thut, G. & Schroeder, C. E. Multisensory integration: flexible use of general operations. *Neuron* **81**, 1240–1253 (2014).
- Stein, B. E., Meredith, M. A., Huneycutt, W. S. & McDade, L. Behavioral indices of multisensory integration: orientation to visual cues is affected by auditory stimuli. *J. Cogn. Neurosci.* **1**, 12–24 (1989).
- McMeniman, C. J., Corfas, R. A., Matthews, B. J., Ritchie, S. A. & Vosshall, L. B. Multimodal integration of carbon dioxide and other sensory cues drives mosquito attraction to humans. *Cell* **156**, 1060–1071 (2014).
- Stein, B. E. & Stanford, T. R. Multisensory integration: current issues from the perspective of the single neuron. *Nature Rev. Neurosci.* **9**, 255–266 (2008).
- Cybenko, G. Approximation by superpositions of a sigmoidal function. *Math. Control Signals Syst.* **2**, 303–314 (1989).
- Duda, R. O. E., H. P. Stork, D. G. *Pattern Classification* (John Wiley and Sons, 2001).
- Hastie, T., Friedman, J. & Tibshirani, R. *The Elements of Statistical Learning* Vol. 2 (Springer, 2009).
- Rigotti, M. et al. The importance of mixed selectivity in complex cognitive tasks. *Nature* **497**, 585–590 (2013).
- Fetsch, C. R., Pouget, A., DeAngelis, G. C. & Angelaki, D. E. Neural correlates of reliability-based cue weighting during multisensory integration. *Nature Neurosci.* **15**, 146–154 (2012).
- Meredith, M. A. & Stein, B. E. Interactions among converging sensory inputs in the superior colliculus. *Science* **221**, 389–391 (1983).
- Meredith, M. A. & Stein, B. E. Descending efferents from the superior colliculus relay integrated multisensory information. *Science* **227**, 657–659 (1985).
- Olcese, U., Iurilli, G. & Medini, P. Cellular and synaptic architecture of multisensory integration in the mouse neocortex. *Neuron* **79**, 579–593 (2013).
- Homborg, U., Christensen, T. A. & Hildebrand, J. G. Structure and function of the deutocerebrum in insects. *Annu. Rev. Entomol.* **34**, 477–501 (1989).

16. Milde, J. J. & Strausfeld, N. J. Cluster organization and response characteristics of the giant fiber pathway of the blowfly *Calliphora erythrocephala*. *J. Comp. Neurol.* **294**, 59–75 (1990).
17. Mu, L., Bacon, J. P., Ito, K. & Strausfeld, N. J. Responses of *Drosophila* giant descending neurons to visual and mechanical stimuli. *J. Exp. Biol.* **217**, 2121–2129 (2014).
18. Basura, G. J., Koehler, S. D. & Shore, S. E. Multi-sensory integration in brainstem and auditory cortex. *Brain Res.* **1485**, 95–107 (2012).
19. Jain, R. & Shore, S. External inferior colliculus integrates trigeminal and acoustic information: unit responses to trigeminal nucleus and acoustic stimulation in the guinea pig. *Neurosci. Lett.* **395**, 71–75 (2006).
20. Lakatos, P., Chen, C. M., O'Connell, M. N., Mills, A. & Schroeder, C. E. Neuronal oscillations and multisensory interaction in primary auditory cortex. *Neuron* **53**, 279–292 (2007).
21. Shore, S. E. Multisensory integration in the dorsal cochlear nucleus: unit responses to acoustic and trigeminal ganglion stimulation. *Eur. J. Neurosci.* **21**, 3334–3348 (2005).
22. Cardona, A. et al. An integrated micro- and macroarchitectural analysis of the *Drosophila* brain by computer-assisted serial section electron microscopy. *PLoS Biol.* **8**, e1000502 (2010).
23. Saalfeld, S., Fetter, R., Cardona, A. & Tomancak, P. Elastic volume reconstruction from series of ultra-thin microscopy sections. *Nature Methods* **9**, 717–720 (2012).
24. Pfeiffer, B. D. et al. Tools for neuroanatomy and neurogenetics in *Drosophila*. *Proc. Natl Acad. Sci. USA* **105**, 9715–9720 (2008).
25. Pfeiffer, B. D. et al. Refinement of tools for targeted gene expression in *Drosophila*. *Genetics* **186**, 735–755 (2010).
26. Li, H. H. et al. A GAL4 driver resource for developmental and behavioral studies on the larval CNS of *Drosophila*. *Cell Rep.* **8**, 897–908 (2014).
27. Hwang, R. Y. et al. Nociceptive neurons protect *Drosophila* larvae from parasitoid wasps. *Curr. Biol.* **17**, 2105–2116 (2007).
28. Ohyama, T. et al. High-throughput analysis of stimulus-evoked behaviors in *Drosophila* larva reveals multiple modality-specific escape strategies. *PLoS ONE* **8**, e71706 (2013).
29. Tsubouchi, A., Caldwell, J. C. & Tracey, W. D. Dendritic filopodia, Ripped Pocket, NOMPC, and NMDARs contribute to the sense of touch in *Drosophila* larvae. *Curr. Biol.* **22**, 2124–2134 (2012).
30. Yan, Z. et al. *Drosophila* NOMPC is a mechanotransduction channel subunit for gentle-touch sensation. *Nature* **493**, 221–225 (2013).
31. Zhang, W., Yan, Z., Jan, L. Y. & Jan, Y. N. Sound response mediated by the TRP channels NOMPC, NANCHUNG, and INACTIVE in chordotonal organs of *Drosophila* larvae. *Proc. Natl Acad. Sci. USA* **110**, 13612–13617 (2013).
32. Robertson, J. L., Tsubouchi, A. & Tracey, W. D. Larval defense against attack from parasitoid wasps requires nociceptive neurons. *PLoS ONE* **8**, e78704 (2013).
33. Tracey, W. D. Jr, Wilson, R. I., Laurent, G. & Benzer, S. *painless*, a *Drosophila* gene essential for nociception. *Cell* **113**, 261–273 (2003).
34. Vogelstein, J. T. et al. Discovery of brainwide neural-behavioral maps via multiscale unsupervised structure learning. *Science* **344**, 386–392 (2014).
35. Xiang, Y. et al. Light-avoidance-mediating photoreceptors tile the *Drosophila* larval body wall. *Nature* **468**, 921–926 (2010).
36. Zhong, L. et al. Thermosensory and nonthermosensory isoforms of *Drosophila melanogaster* TRPA1 reveal heat-sensor domains of a thermoTRP Channel. *Cell Rep.* **1**, 43–55 (2012).
37. Schrader, S. & Merritt, D. J. Central projections of *Drosophila* sensory neurons in the transition from embryo to larva. *J. Comp. Neurol.* **425**, 34–44 (2000).
38. Zlatic, M., Li, F., Strigini, M., Grueber, W. & Bate, M. Positional cues in the *Drosophila* nerve cord: semaphorins pattern the dorso-ventral axis. *PLoS Biol.* **7**, e1000135 (2009).
39. Grueber, W. B. et al. Projections of *Drosophila* multidendritic neurons in the central nervous system: links with peripheral dendrite morphology. *Development* **134**, 55–64 (2007).
40. Klapoetke, N. C. et al. Independent optical excitation of distinct neural populations. *Nature Methods* **11**, 338–346 (2014).
41. Ernst, M. O. & Bulthoff, H. H. Merging the senses into a robust percept. *Trends Cogn. Sci.* **8**, 162–169 (2004).
42. Kenshalo, D. R., Iwata, K., Sholas, M. & Thomas, D. A. Response properties and organization of nociceptive neurons in area 1 of monkey primary somatosensory cortex. *J. Neurophysiol.* **84**, 719–729 (2000).
43. Mendell, L. M. Physiological properties of unmyelinated fiber projection to the spinal cord. *Exp. Neurol.* **16**, 316–332 (1966).
44. Ohshiro, T., Angelaki, D. E. & DeAngelis, G. C. A normalization model of multisensory integration. *Nature Neurosci.* **14**, 775–782 (2011).
45. Bargmann, C. I. & Marder, E. From the connectome to brain function. *Nature Methods* **10**, 483–490 (2013).
46. White, J. G., Southgate, E., Thomson, J. N. & Brenner, S. The structure of the nervous system of the nematode *Caenorhabditis elegans*. *Phil. Trans. R. Soc. Lond. B* **314**, 1–340 (1986).
47. Bock, D. D. et al. Network anatomy and *in vivo* physiology of visual cortical neurons. *Nature* **471**, 177–182 (2011).
48. Briggman, K. L., Helmstaedter, M. & Denk, W. Wiring specificity in the direction-selectivity circuit of the retina. *Nature* **471**, 183–188 (2011).
49. Kim, J. S. et al. Space-time wiring specificity supports direction selectivity in the retina. *Nature* **509**, 331–336 (2014).
50. Takemura, S. Y. et al. A visual motion detection circuit suggested by *Drosophila* connectomics. *Nature* **500**, 175–181 (2013).

**Supplementary Information** is available in the online version of the paper.

**Acknowledgements** We thank G. Rubin and the Janelia Fly EM Project for the gift of the comprehensive image dataset of the larval nervous system; S. Lauchie and A. Brothers for assistance with EM imaging; B. Arruda and T. Dang for assistance with behavioural screens; L. Herren, I. Andrade, K. Floria and A. Berthold van der Bourg for assistance with neuronal reconstruction; G. Rubin, H. Dionne and B. Pfeiffer for GAL4 and Split GAL4 lines; A. Nern and G. Rubin for the single cell FLP-out stocks; J.-M. Knapp for *Tsh-LexA* stock; H.-H. Li and Janelia Fly Light Project Team for images of neuronal lines; K. Hibbard, M. Mercer, T. Laverty and the rest of Janelia Fly Core for stock construction and fly crosses; G. Denisov for the roll and crawl detection LARA software; E. Trautman, R. Svirskas, C. Weaver and D. Olbris for data analysis pipelines; Y. Park, C. Priebe, D. Naiman and J.-B. Masson for advice on statistical analysis; V. Jayaraman for input on calcium imaging; and W. Denk, B. Dickson, S. Druckmann, B. Gerber, K. Svoboda and C. Zuker for helpful comments on the manuscript. We thank Janelia HHMI for funding. A.C. and C.M.S.-M. were also funded by the Institute of Neuroinformatics of the University of Zurich and ETH Zurich, the SNSF grant 31003A\_132969, the Universität Zürich Forschungskredit, and the HHMI Visiting Scientist program at Janelia. The EM image data is available via the Open Connectome Project (<http://www.openconnectomeproject.org>).

**Author Contributions** T.O., C.M.S.-M., A.C. and M.Z. conceived the project, analysed the data and wrote the manuscript. T.O. performed and analysed behavioural and functional imaging experiments. C.M.S.-M., J.V.A. and A.C. performed neuronal reconstructions. A.C. registered the L1 volume. J.W.T. analysed the expression patterns of all the GAL4 lines and intersections for targeting of single cell types. R.D.F. generated the EM image data. M.R.A. and K.B. wrote the JAABA roll detection pipeline and performed statistical analysis. J.H.S. supported the generation of the *abd*.1.5 dataset. R.F. provided critical suggestions for functional imaging experiments. C.M.S.-M. built the model. B.D.M. provided critical input and helped with writing the manuscript.

**Author Information** Reprints and permissions information is available at [www.nature.com/reprints](http://www.nature.com/reprints). The authors declare no competing financial interests. Readers are welcome to comment on the online version of the paper. Correspondence and requests for materials should be addressed to A.C. (cardonaa@hhmi.org) or M.Z. (zlatim@hhmi.org).

## METHODS

**Fly strains.** In the main text and figures, short names are used to describe genotypes for clarity. The complete genotypes of animals used in this study are shown in Supplementary Table 2.

The following strains from the Rubin GAL4/LexA collection were used for the figures in the manuscript: R61D08-GAL4, R69F06-GAL4, R72F11-GAL4, R20B01-GAL4, R71A10-GAL4, R57F07-GAL4, R47D07-GAL4, R16E11-LexA, R61D08-LexA, R72F11-LexA and the control stock *w<sup>+</sup>*;*attP2* with no GAL4 or LexA<sup>24,51</sup>. For the thermogenetic activation screen we selected 586 GAL4 lines<sup>26</sup> that drove expression in relatively few neuron types (one to five) and used them to drive expression of TRPA with UAS-dTRPA1<sup>22,52</sup>.

The following effector stocks were used: pJFRC25-13xLexAop2-IVS-dTrpA1 in *vk05*<sup>25,54</sup>; pJFRC48-13xLexAop2-IVS-mrytdTomato in *attP18*, pJFRC20-8xLexAop2-IVS-GAL80-WPRE in *attP18*<sup>25,54</sup>; pJFRC29-10xUAS-IVS-mry::GFP-p10 in *attP2*<sup>54</sup>; pGP-JFRC7-20xUAS-IVS-GCaMP6s<sup>55</sup> (Bloomington stock no. 42749); pGP-JFRC7-20xUAS-IVS-GCaMP6f5 (Bloomington stock no. 52869); 20xUAS-IVS-GCaMP3 (Bloomington stock no. 32236;<sup>56</sup>) and UAS-JFRC12-10xUAS-mryGFP (Bloomington stock no. 32197;<sup>51,54</sup>) were gifts from B. D. Pfeiffer, G. Rubin, and the GECI project team (HHMI Janelia Research Campus). *ppk1.9-GAL4*<sup>57</sup> was a gift from D. Tracey (Duke University). *ppk1kb-hs43-lexA-GAD* in *attP40* was a stock that was previously described in ref. 34. UAS-dTRPA1<sup>52</sup> was a gift from P. Garrity. UAS-EGFP-Kir2.1<sup>58</sup> was outcrossed to *w<sup>1118</sup>* and gifted from D. Sitaraman (Yale University). LexAop2-P2X<sub>2</sub><sup>59</sup> was a gift from C.-H. Yang (Duke University; unpublished stock).

For selective targeting the Goro neurons, we used LexAop-FLP; UAS>stop>dTrpA1::myc<sup>60</sup> a gift from B. Dickson, crossed with *w<sup>1118</sup>*;16E11-LexA (*attP40*; R69F06-GAL4 (*attP2*), which drives expression in Goro neurons. The expression was determined by anti-Myc antibody (seen on immunohistochemistry).

*Tsh-LexA* was a gift from J.-M. Knapp and J. Simpson (unpublished stock). In brief, the *tsh-LexA* driver is an enhancer trap inserted into the 5' UTR of the *tsh* locus. It was generated via a P-element swap that replaced the *p(GawB)* insertion of *tsh-GAL4*<sup>61</sup> with *P(UpP65L)* and the enhancer-trap LexA construct. Proper targeting and orientation of *P(UpP65L)* were confirmed by splinkerette PCR and sequencing by J.-M. Knapp (unpublished results).

LexAop2-mry-TDTomato-p10 (*attP40*), a gift from D. Mellert (HHMI Janelia Research Campus; unpublished stock), is an *mry*:TDtomato fragment with AcNPV *p10*<sup>54</sup>. To selectively target Basin-4 neurons we generated a Split-GAL4<sup>25,62</sup> stock R72F11\_AD inserted in *attP40* (chromosome 2L) and 57F07\_DBDB in *attP2* (3L). AD and DBDB combinations were assembled in a *w<sup>1118</sup>* background. We identified R57F07 as a candidate line for this intersection because its activation also evoked rolling in the thermogenetic activation screen (Extended Data Fig. 4). Stochastic labelling of single cells in R57F07 and R72F11, using a FLP-based strategy (see below) revealed they both drive expression in Basin-4. R57F07 also drove expression in other neurons in the tip of the nerve cord and brain (Extended Data Fig. 4).

The 'FLP-out' approach<sup>63</sup> for stochastic single-cell labelling will be described in detail elsewhere (Nern *et al.*, manuscript in preparation). In brief, heat-shock induced expression of FLP recombinase was used to excise FRT-flanked interruption cassettes from UAS reporter constructs carrying HA, V5, and Flag epitope tags, and stained with epitope-tag specific antibodies. This labelled a subset of the cells in the expression pattern with a stochastic combination of the three labels.

**Behavioural apparatus.** The apparatus comprises a video camera (DALSA Falcon 4M30 camera) for monitoring larvae, a ring light illuminator (Cree C503B-RCS-CW0Z0AA1 at 624 nm in the red), a computer (see ref. 28 for details; available upon request are the bill of materials, schematic diagrams and PCB CAM files for the assembly of the apparatus) and two hardware modules for controlling vibration and temperature (Oven Industries PA, Model 0805). Both hardware modules were controlled through multi worm tracker (MWT) software (<http://sourceforge.net/projects/mwt>), as described in ref. 28.

The module for presenting vibration consists of a speaker (120 W, 12 inches in diameter) and an amplifier (Pyle Pro PCA3) controlled by a signal generator (Tektronix AFG3021B). The speaker was used to generate vibrations between 100 and 1000 Hz, with an electronic signal (1 V, 100 Hz) generating a sound pressure level of 122 dB at the assay plate (measured by a Realistic 33-2050 Sound Level Meter). The frequency of vibration at the agar surface and vibration intensity (measured as acceleration in m s<sup>-2</sup>) was measured with an ADXL345 3-axis accelerometer assembled onto a small printed circuit board placed on the agar as described in ref. 28.

For thermal activation, we used a Peltier module controlled by a temperature controller (Oven Industries PA, Model 0805). An aluminium plate covered with a thin layer of 4% charcoal agar was placed on the Peltier module. The temperature

of the agar was raised from 20 °C to 30 °C/32 °C to weakly/strongly activate the dTRPA1 channel. By using a temperature gun, we confirmed that the agar reached the Peltier tile setting temperature. The time to reach the target temperature ranged from 3 to 8 s. The behaviour rigs were inside 32.00" wide × 28.00" deep × 60.00" high temperature-controlled enclosures with temperature settable from ambient to 40 °C in 0.1 °C steps (Life Science Engineering, Inc.). The humidity in the room was monitored and held at 58%, with humidifiers (Humidifirst Mist Pac-5 Ultrasonic Humidifier).

**Behavioural experiments.** Embryos were collected for 6 h at 18 °C and 65% humidity. Larvae containing the UAS-dTrpA1 or LexA-dTrpA1 transgene were raised at 18 °C for 7 days with normal cornmeal food. Foraging third instar larvae were used for all experiments. Larvae containing the UAS-CsChrimson transgene were grown in the dark at 25 °C for 4 days on fly food containing *trans*-retinal (Sigma, R2500) at a concentration of 500 M.

Before the experiments, the larvae were separated from food by using 15% sucrose and washed with water. The larvae were then dried and placed in the center of the arena. The substrate for the behavioural experiments was 3% Bacto agar gel in a 25 × 25 cm square plastic plate for experiments involving thermal activation and vibration stimuli, or a 10 × 10 cm plate for those involving thermal activation alone. We tested approximately 15–50 larvae at once in the behavioural assays. The temperature of the entire rig was kept at 25 °C (for optogenetic activation experiments) or 30 °C or 32 °C for thermogenetic activation experiments. The agar plates were also kept at the desired temperature prior to experiment. For optogenetic activation experiments we exposed dishes of larvae to red light (630 nm, 2.4 mW per cm<sup>2</sup>). Optogenetic activation offers greater temporal precision than thermogenetic activation so we used to study the ability of Basin, Goro and A00c neurons to trigger the entire behavioural sequence roll-fast crawl, or just a single element of the sequence (roll or crawl).

The MWT software<sup>64</sup> (<http://sourceforge.net/projects/mwt>) was used to record all behavioural responses and to control the presentation of vibration stimuli.

For the thermogenetic activation screen we used 586 GAL4 lines preselected for expression in relatively few neuron types (one to five) to drive expression of dTRPA1. In each experiment, we exposed dishes of larvae to 32 °C to thermogenetically activate dTRPA1-expressing neurons. We detected 32 'hits' that contained neurons whose thermogenetic activation evoked rolling in a significant fraction of animals. We analysed further hits that evoked rolling in the highest fraction of larvae and that drove expression in the least neuron types.

**Behaviour quantification.** Larvae were tracked in real-time using the MWT software. We rejected objects that were tracked for less than 5 seconds or moved less than one body length of the larva. For each larva MWT returns a contour, spine and centre of mass as a function of time. Raw videos are never stored. From the MWT tracking data we computed the key parameters of larval motion, using specific choreography (part of the MWT software package) variables<sup>28</sup>. From the tracking data, we detected and quantified crawling and rolling events and the speed of peristaltic crawling strides as described in ref. 28, using the LARA software package (<http://sourceforge.net/projects/salam-hhmi>). We also trained a machine-learning classifier, using JAABA (Janelia Automatic Animal Behavior Annotator<sup>65</sup>) to detect rolling events from the tracking data. The false detection rate of the JAABA rolling classifier was slightly smaller (2.8%, *n* = 89) than that of the LARA detection software (3.6%), but the results obtained with both methods were very similar. The MATLAB code for the rolling classifier is available upon request. The data presented is a quantification of rolling events detected with JAABA. To calculate the percentage of animals that rolled in response to thermogenetic activation, vibration, or both, we selected for analysis all the animals that were tracked throughout the entire 15-second sampling interval following stimulation. We then calculated the percentage of animals from this sample for which at least one rolling event was detected during the 15-second interval. The instantaneous percentage of rolling and crawling larvae (Extended Data Fig. 7a) as a function of time was calculated by dividing the number of larvae performing rolling at each time point with the total number of larvae tracked at each time point.

**Selective targeting of Goro neurons.** We expressed FLP selectively in the Goro neurons using the weak 16E11 LexA lines (in 16ElexA/LexAop FLP; UAS>stop>UAS-dTRPA1::myc/R69F06). Selectively in Goro neurons, FLP stochastically excises the STOP cassette that prevents the expression of UAS-dTRPA1. Now the strong R69F06 promoter can drive high levels of dTRPA1 expression, selectively in Goro neurons. Since this method of Goro activation is stochastic we monitored rolling in response to 32 °C exposure in individual larvae. We dissected all animals, noted whether they rolled or did not, and stained their nervous systems with anti-Myc, to identify those that had Goro expression.

**Statistical analysis.** Statistical analysis was performed using MATLAB (MathWorks) software. The calcium responses in the paired trials shown in Fig. 4f were compared both using the paired *t*-test and Wilcoxon signed-rank

test. Required sample size for power 0.8 was determined using GPower software for paired *t*-test and for a large pre-specified effect size based on a few pilot trials. Indeed the effect size in the data was large ( $P = 0.016$  and  $d = 1.05$  for one-sided paired *t*-test and  $P = 0.02$  and  $r = 0.81$  using Wilcoxon signed-rank test). The speed of peristaltic crawling strides was compared using Wilcoxon rank sum test (and Bonferroni correction for multiple comparisons). In all figures, \* and \*\* represent  $P < 0.05$  and  $P < 0.01$ , respectively. Required sample size for power 0.8 was determined using GPower software for a medium pre-specified effect size. The fractions of animals that rolled under the different experimental conditions were compared using the  $\chi^2$  test. *P* values were corrected for multiple comparisons using Bonferroni correction. Power analysis was performed as described below.

We performed an analysis of the power of our statistical tests of behavior differences, given the sample sizes and effect sizes observed. In addition, we computed the minimum effect sizes our analyses would have been sensitive to with a power 0.95, given the sample sizes. In our power analyses, we assumed that the distribution of the fraction of larvae that rolled for the control populations,  $q_0$ , was known and equal to the fraction measured in a large number of trials.

For each experiment, we tested the null hypothesis that the fraction of experimental animals that rolled was less, more, or equal to the control fraction, depending on the type of experiment. For example, when activating the Goro neurons, we tested whether we could reject the null hypothesis that the fraction of larvae that rolled was less than or equal to the control fraction. In this case, assuming that each animal is an independent sample from the same distribution, the number of larvae rolling follows a binomial distribution. Thus, if the null hypothesis is that the experimental larvae roll at most as much as control, the probability that the null hypothesis holds can be computed from the binomial cumulative distribution function:

$$\Pr_{\leq q_0}(n, \hat{q}n) = 1 - \text{binocdf}(\hat{q}n, q_0)$$

Where  $n$  is the number of experimental larvae tested,  $\hat{q}$  is the measured fraction that roll, and  $\text{binocdf}(k, r)$  is the binomial cumulative distribution function. We assumed we would reject the null hypothesis if this probability was less than 0.01. For a given  $q_0$  and  $n$ , we can thus compute  $\hat{q}_{q_0, n}^*$ , the minimum  $\hat{q}$  such that we would reject the null hypothesis using this equation.

To compute the power of this statistical test given the sample size  $n$  and true fraction of experimental larvae expected to roll  $q$ , we assumed that our collected experimental data were independent draws from the Bernoulli distribution with parameter  $q$ , and computed the probability that our observed fraction of

$$\Pr(\text{reject null hypothesis} | q_0 \leq q, n) = 1 - \text{binocdf}\left(\hat{q}_{q_0, n}^* n, q_0\right)$$

Analogous equations were used for testing whether the experimental rolled at least as much as control or the same amount as control.

Using these equations, we computed the power of each statistical test given the observed sample size  $n$ , control fraction that rolled  $q_0$ , and the experimental fraction that rolled  $q$ , for each set of experiments. We also computed the minimum effect size  $q/q_0$  that would be sensitive with power 0.95, given the observed sample size  $n$  and control fraction that rolled  $q_0$ . These results are listed in Supplementary Tables 1 and 3.

**Immunohistochemistry.** The following antibodies were used: rabbit anti-GFP (1:1000, A11122, Invitrogen), rat anti-N-Cad (1:50, Developmental Studies Hybridoma Bank), mouse anti-nc82 (1:20; Developmental Studies Hybridoma Bank), mouse anti-Myc (9E10, 1:20, Developmental Studies Hybridoma Bank), rabbit anti-HA-Tag (1:300, Cell Signaling, #3724), rat anti-FLAG (1:200, NOVUS, NPP1-06712), mouse anti-V5 Dylight549 (1:400, AbD Serotec, MCA1360D549). For secondary antibody Alexa Fluor 488 goat anti-rabbit IgG (1:200, Invitrogen), Alexa Fluor 568 goat anti-mouse IgG (1:200, Invitrogen) and Alexa Fluor 488 goat anti-mouse IgG (1:200, Invitrogen) were used.

The central nervous systems of wandering third instar larvae were dissected in cold Schneiders Insect medium (Sigma, S0146) and fixed in 4% phosphate-buffered saline (PBS) with 4% paraformaldehyde (Electron Microscopy Science) at room temperature for 20 min. After washes in 0.4% Triton X-100 in PBS, samples were preblocked with 3% normal goat serum (NGS) in for 30 min at room temperature. The samples were then incubated in primary antibody for 2 to 3 days at 4 °C. After extensive washes in 0.4% Triton X-100 in PBS, the samples were incubated at 4 °C for 2 days in a secondary antibody solution. After further extensive washes, the samples were rinsed in PBS, dehydrated through an EtOH series, cleared in Xylene and mounted in DPX mountant (Sigma-Aldrich). Images were taken with a 710 or 700 laser-scanning confocal microscope (Zeiss) under 20× 0.8 NA or 63×, 1.4 NA objective and processed in ImageJ software<sup>66</sup> (NIH).

**Functional connectivity assay (GCaMP recording).** For activation of presynaptic neurons (MD IV, chordotonal, Basins or A05q) with the ATP-gated P2X<sub>2</sub> channel and imaging in postsynaptic neurons (Basins, Goro, A00c or A05q), the central nervous system of wandering third instar larvae were dissected out in cold physiological saline containing 103 mM NaCl, 5 mM KCl, 5 mM HEPES, 26 mM NaHCO<sub>3</sub>, 1 mM NaH<sub>2</sub>PO<sub>4</sub>, 5 mM Trehalose, 6 mM sucrose, 2 mM CaCl<sub>2</sub> 2 mM H<sub>2</sub>O, 8 mM MgCl<sub>2</sub> 6 mM H<sub>2</sub>O, and kept stable by sticking them on poly-L-lysine (SIGMA, P1524) coated cover glass placed in small Sylgard (Dow Corning) plates. A borosilicate pipette (1 to 2 μm tip diameter) filled with 5 mM adenosine 5'-triphosphate (ATP, Amersham 27-1006) and 50 g ml<sup>-1</sup> Alexa Fluor 594 hydrazide (Invitrogen, A10438) dye in physiological saline was positioned 3 to 5 μm from the axon terminals of the target presynaptic neurons expressing the ATP-gated P2X<sub>2</sub> channel and dsRed and the ATP solution was pressure-ejected using a Picospritzer (Parker Hannifin Co.).

When ejecting ATP onto the axon terminals of MD IV or chordotonal neurons, we imaged calcium transients in the dendritic arbor of the Basin neurons, not the cell bodies (which in the insect are removed from the neuropil). When stimulating Basins in abdominal segments, by ejecting ATP onto their axon terminals in ventral nerve cord, we imaged calcium transients in the dendrites of Goro (in dorsal thoracic nerve cord), or in axon terminals of A05q (in dorsal nerve cord) and A00c (in the brain). When stimulating A05q by ejecting ATP onto their dendrites in ventral nerve cord in abdomen, we imaged calcium transients in Goro dendrites in dorsal thoracic nerve cord.

Puffs were 25 ms in duration, and the pressure was adjusted so that red fluorescence (from the Alexa 594) ejection could be seen clearly while imaging. The same stimulus was presented every 30 sec for a total of three trials in each experiment.

When vibration stimuli were also used in experiments, rather than only P2X<sub>2</sub> activation, the larvae were dissected using methods similar to those described previously for neuromuscular junction<sup>67</sup> on the Sylgard plate. In brief, larvae were cut up along the dorsal body wall midline and then opened by placing dissection pins. The cell bodies of abdominal peripheral sensory neurons and their nerves were kept intact. The anterior tips were removed, and the CNS was attached to a poly-L-lysine coated cover glass. For vibration stimuli in the two-photon rig, we embedded piezo extension actuators (Piezo System Inc., Model Q220-A4-303XE) in the Sylgard plate and used TTL pulses from the Prairie View software to control the timing of stimulation. The acceleration was measured with an ADXL345 3-axis accelerometer<sup>28</sup>. The vibration stimuli were 1,000 Hz and 6.67 m s<sup>-2</sup>, 15 sec long. The same stimulus was presented every 30 sec for a total of three trials in each experiment. For comparing the responses of Basin-4 to combined activation (nociceptor activation with P2X<sub>2</sub> and ATP injection plus vibration) to nociceptor activation or vibration alone (Figure 4d and e), each trial consisted of ATP injection, vibration, and a combination (ATP injection and vibration), with 30 sec between each stimulation. Three such triplet trials were presented in each experiment.

We performed imaging on a Prairie Technologies two-photon microscope using an Olympus 60× 0.8 NA objective. A mode-locked Ti:Sapphire Chameleon Ultra II laser (Coherent) tuned to 925 nm was used for excitation. Fluorescence was collected with photomultiplier tubes (Hamamatsu) after band-pass filtering. Images were acquired in frame-scan mode (maximum speed, 1,215 f.p.s.) for a single plane of the CNS.

**GCaMP image analysis.** Image data were processed by ImageJ software<sup>66</sup> (NIH) and analysed using custom code written in MATLAB (MathWorks). Specifically, regions of interest (ROIs) were determined by averaging the ten frames before stimulation and segmenting this data by the function MEAN<sup>68</sup> in ImageJ. The mean intensity of the ROI was measured in ImageJ. In all cases, changes in fluorescence were calculated relative to baseline fluorescence levels ( $F_0$ ) as determined by averaging over a period of at least 3 sec just before ATP puff or vibration stimulation.  $\Delta F/F_0$  values were calculated as  $\Delta F/F_0 = (F_t - F_0)/F_0$ , where  $F_t$  is the fluorescent mean value of a ROI in a given frame. Peak  $\Delta F/F_0$  is the maximum value in the 5 sec window following stimulus onset.

**Electron microscopy preparation and imaging.** For generating the electron microscopy dataset comprising 1.5 abdominal segments (segment a2 and a3), the central nervous systems from 12–24-h-old wild-type *w<sup>1118</sup>* first instar larvae were manually dissected out in PBS, and immediately transferred to 2% glutaraldehyde in 0.1 M sodium cacodylate, pH 7.4 buffer. Samples were post-fixed in 1% OsO<sub>4</sub> in the same buffer and stained en bloc with 1% aqueous uranyl acetate before subsequent dehydration in ethanol and propylene oxide, and embedding in Epon. Serial 45 nm sections were cut with a Leica UC6 ultramicrotome using a Diatome diamond knife, and picked up with Synaptek slot grids with Pioloform support films. Sections were stained with uranyl acetate followed by Sato's lead<sup>69</sup>.

For generating the electron microscopy dataset comprising the entire central nervous system, central nervous systems from 6-h-old [iso] Canton S G1 x *w<sup>1118</sup>*

[iso] 5905 female larvae were manually dissected out in PBS. The isolated central nervous systems were immediately transferred to 125 µl of 2% glutaraldehyde in 0.1 M sodium cacodylate buffer, pH 7.4 in a 0.5 dram glass vial (Electron Microscopy Sciences, cat. no. 72630-05) to which an equal volume of 2% OsO<sub>4</sub> in 0.1 M sodium cacodylate buffer, pH 7.4 was added and gently mixed. Each CNS was then fixed in an ice bath in a Pelco BioWave PRO microwave oven (Ted Pella, Inc.) at 350-W, 375-W and 400-W pulses for 30 sec each, separated by 60-sec intervals with the microwaves off. Samples were rinsed 3 × 30 sec at 350 W with 0.1 M sodium cacodylate buffer, separated by 60-sec intervals with the microwaves off, and post-fixed with 1% OsO<sub>4</sub> in 0.1 M sodium cacodylate buffer at 350-W, 375-W and 400-W pulses for 30 sec each, separated by 60-sec intervals with the microwaves off. After rinsing with distilled water 3 × 30 sec at 350 W with 60-sec pauses between pulses, the samples were stained en bloc with 1% uranyl acetate in water by microwave at 350 W for 3 × 30 sec with 60-sec pauses between microwave pulses. The samples were then dehydrated in an ethanol series followed by propylene oxide, infiltrated and embedded with EPON resin. Serial 50-nm sections were cut with a Leica UC6 ultramicrotome using a Diatome diamond knife, and picked up with Synaptek slot grids with Pioloform support films with 2 nm of carbon (C). Sections were stained with uranyl acetate followed by Sato's lead<sup>49</sup>.

Both data sets were imaged using Leginon<sup>70</sup>, the 1.5 abdominal segment on an FEI T20 TEM (Hillsboro) at 4.4 nm × 4.4 nm pixel resolution, the complete L1 brain on an FEI Spirit TEM at 3.8 nm × 3.8 nm pixel resolution. The resulting images were montaged and registered using the nonlinear elastic method described in ref. 23.

**Neuronal reconstruction.** Reconstructions were made in a modified version of CATMAID<sup>71</sup> (<http://www.catmaid.org>). The process of reconstructing neurons in CATMAID involves starting with a specified neurite in a section of the electron microscopy data, and manually building a 3D skeleton representation of the neuronal morphology and the location of synaptic active zones and synaptic partners.

The synaptic connections mapped and reported in this study all represent fast, chemical synapses. Synapses must match several criteria over multiple adjacent sections: a thick black active zone, vesicles, and presynaptic specializations, such as a T-bar, on the presynaptic side, and evidence of postsynaptic membrane specializations<sup>72</sup>.

To identify sensory axons, reconstruction was initiated at the entry point of nerves into the neuropil. Sensory neurons project ventrally in the nerve cord, and motor neurons project dorsally<sup>37,38,73</sup>, so the sensory axons were readily identified in the ventral portion of the nerve root. All sensory axons were traced and MD IV and chordotonal axons were recognized based on their distinguishing features, previously described using confocal microscopy imaging<sup>37,38,74</sup>. Chordotonal projections were readily identified based on the characteristic intermediate location of their terminals in the mediolateral axis and the dorsoventral axis of the nervous system. We found that all eight chordotonal axons were already tightly bundled together in the nerve root. The MD IV projections were readily recognized based on the characteristic medial-most and ventral-most location of their terminals. Neuronal partners of the eight chordotonal axons and the three MD IV axons in both hemisegments were reconstructed by initiating reconstructions at the site of every postsynaptic target in all chordotonal terminals until all targets were exhausted. A review of all skeletons was done by CMSM to identify incorrect or missed branches and synapses.

In the comprehensive L1 electron microscopy volume, Basin cells in A1 and A4 segments were found using landmarks such as cell body position, the entry point of primary neurite into the neuropil, and branch points on the primary neurite. In brief, the Basin lineage was first recognized on the basis of the characteristic cell body location (lateral intermediate), the trajectory of their primary neurite which is parallel to the entering nerve, and the neuropil entry point of the lineage, as well as the pattern of the low-order, large branches. The lineage contains more cells than just the four Basins, but the other cells have very different projection patterns. The Basins in the A1 segment were identified by tracing the primary and secondary neurites of multiple members of the lineage and abandoning those that did not have the distinguishing features of the Basins. The four Basins in each hemisegment were reconstructed in full and individual Basins recognized based on their unique features (see Extended Data Fig. 2). Basin targets were reconstructed by tracing exhaustively downstream of all presynaptic sites in Basin axons. Goro neurons were found in a similar way as Basins. Starting with high-resolution 3D image stacks of single cells (visualized using the FLP-based strategy described above), we looked at the cell body location, primary neurite projection, and major branch points. We then traced neurites consistent with the primary neurite projection and cell body location until finding only two individual cells, one in each hemisegment of segment T2, with branch points consistent with Goro neurons. Completed reconstructions were then checked for consistency with light

data in axon and dendritic projections. Partial reconstructions of sibling neurons, as well as homologous neurons in adjacent thoracic segments, resulted in morphologies very different from that of Goro neurons as observed by light microscopy, indicating that only two neurons in the whole of the thorax match the expected morphological pattern. Descending neurons were found by reconstruction of neurons upstream of synaptic inputs in Goro dendrites. A subset of fourth-order neurons was found by reconstructing downstream of all synaptic output sites of only one of the ascending third-order A00c-a4 neurons. Left and right homologues of reconstructed neurons were identified by considering a suite of morphological and synaptic features, focusing on neuropil entry location, primary branch locations, and the location of pre- and postsynaptic sites.

Neuronal morphologies were analysed in MATLAB using custom scripts. Circuit diagrams were made in Gephi<sup>75</sup> and edited in Adobe Illustrator CS6 (Adobe Systems, Inc.).

**Validation of methodology of electron microscopy reconstruction.** In *Drosophila*, as in other insects, the gross morphology of many neurons is stereotyped and individual neurons are uniquely identifiable based on morphology<sup>37,50,76,77</sup>. Furthermore, the nervous system in insects is largely bilaterally symmetric and homologous neurons are reproducibly found on the left and the right side of the animal. In this study we therefore validate the wiring diagram by: (1) independently reconstructing partners of homologous neurons on the left and right side of the nervous system; (2) independently reconstructing partners of homologous neurons in EM volumes from two different individuals; (3) performing functional connectivity experiments to validate some key connections predicted by the wiring diagram.

**Validating the wiring diagram by independent reconstruction on the left and right.** By randomly re-reviewing annotated synapses and terminal arbors in our dataset we estimated the false positive rate of synaptic contact detection to be 0.0167 (1 error per 60 synaptic contacts). Assuming the false positives are uncorrelated, for an  $n$ -synapse connection the probability that all  $n$  are wrong (and thus that the entire connection is a false positive) occurs at a rate of 0.0167<sup>n</sup>. Thus, the probability that a connection is false positive reduces dramatically with the number of synaptic connections contributing to that connection.

Even for  $n = 2$  synapse connections, the probability that the connection is not true is 0.00028 (once in every 3,586 two-synapse connections) and we call connections with two or more connections 'reliable' connections. Similarly, the probability that even a one-synapse connection annotated between homologous neurons both on the left and on the right side of the nervous system is not true is 0.00028. The probability that a false-positive connection with two synapses is observed twice between the same cell types is even lower (0.000282). Because false-positive synapses between a single pair of homologous neurons could potentially be correlated (due to mis-annotation of a single branch with multiple contacts), we perform extra rounds of focused re-review of the arbors associated with connections in our wiring diagram with less than four synapses to confirm that they are neither mis-annotated synapses or incorrect branches. Furthermore, while false positives between a single pair of homologous neurons could potentially be correlated, the false positives between different pairs of homologous neurons (on the left side and the right side) cannot be correlated (they are not on the same branch). Thus the probability that reliable (with two or more synapses) and reproducible (found between both the left and right homologues within an individual) connections are not true is extremely low and we are highly confident in such connections. All the connections discussed in this study and all the principles derived from the wiring diagram are based on such reliable and reproducible connections.

False negatives are far more common in our reconstructions than false positives. We were able to trace 81.5% (1,676/2,054) of postsynaptic sites downstream of Basins back to identifiable neuronal arbors, leaving 18.5% (378/2,054) of synaptic outputs associated with small, unidentifiable arbor fragments due to ambiguities in the data. The majority have only a single synaptic input from Basins (163/231 fragments), and only 8/231 fragments have five or more Basin inputs. If the synapses that could not be associated with identified neurons were distributed randomly, the likelihood of completely omitting a connection with  $n$  synapses is approximately 0.185<sup>n</sup>, which is 0.006 for  $n = 3$ . Thus the likelihood that we have completely omitted a three-or-more-synapse connection is quite low.

**Reproducibility of the wiring diagram across different individuals.** For a connection in the wiring diagram to be useful for future physiological and behavioural experiments in different individuals, it should not just be correctly identified in one animal, but it should be generalizable across animals. We therefore assessed the extent to which the connections in this wiring diagram are reproducible across individuals.

For this study we obtained electron microscopy volumes from two different larvae: one comprising 1.5 nerve cord segments (a2/a3), and one comprising the

entire nervous system. We reconstructed the chordotonal and MD IV sensory neurons, the Basin neurons and all the other partners downstream of both the nociceptive and the sensory neurons in both electron microscopy volumes. In the smaller abd1.5 volume some of the downstream neurons had a large fraction of their arbor outside the volume and were not identifiable, whereas others were mostly confined within the electron microscopy volume and were uniquely identifiable based on key morphological features. We could therefore assess the reproducibility of connections between homologous neurons present and uniquely identifiable in both volumes across two individuals (Extended Data Fig. 3). We identified connections between neuron types that have at least two synapses and for which a connection with at least two synapses also exists between homologous neuron types on the other side of the same individual. 100% ( $n = 36$ ) of connections with at least two synapses per connection that were reproducible across the same individual were also reproducible across individuals; that is, those connections also existed on both sides in the other individual.

If we consider each individual sensory neuron in a hemisegment as unique, we find a total of 76 connections (38 pairs of connections) between individual neurons with at least two synapses between homologues on both the left and right of the same individual. In 100% of cases in which a connection was present between homologues on both sides in one animal it was also present between homologues in the other animal, at least on one side. 96% of connections with at least two synapses that existed between homologous neurons on both sides in one animal also existed between homologues on both sides in the other animal. 4% of connections with at least two synapses present between homologues on both sides in one animal were not present between homologues in the other animal on the same side, but a connection was present between homologues on the other side (in the other hemisegment) in the other individual (see Extended Data Fig. 3 for more details).

Together with the above error rates, the observed reproducibility of connections across individuals gives us strong confidence that the observation of a reliable connection in one animal both measures a real connection in that individual and predicts similar connectivity in other animals.

**Functional validation of connections mapped using electron microscopy reconstruction.** Another way to validate a wiring diagram is to functionally test the connections obtained with electron microscopy reconstruction. If the anatomical and functional connectivity studies are done in different individuals this provides further validation of the reproducibility and generalizability of the wiring diagram. In this study we were able to generate reagents to functionally test a number of anatomical connections predicted by the wiring diagram. By activating the presynaptic partner and monitoring calcium transients in the direct post-synaptic partner we tested the following reproducible direct anatomical connections with, on average, five or more synapses per connection:

- MD IV onto Basin-4 (average >10 synapses per connection) (Fig. 3b)
- Chordotonal onto Basins (average >10 synapses per connection) (Extended Data Fig. 4d)
- Basins onto A00c (average >10 synapses per connection) (Extended Data Fig. 6j)
- Basins onto A05q (average >5 synapses per connection) (Extended Data Fig. 6e)
- A05q onto Goro (average 5 synapses per connection) (Extended Data Fig. 6g)

For the anatomical connection from MD IV onto Basin-1 with only two synapses per connection on average, the functional connectivity experiments did not reveal a functional excitatory connection (Fig. 3a).

**Model of multilevel convergence.** The model consists of two sensory inputs processed in two layers (Extended Data Fig. 8a). The sensory inputs, chordotonal and MD IV, have activity  $E_{\text{Mech}}$  and  $E_{\text{Noci}}$  respectively. Sensory input intensity can range from 0–100 (arbitrary units), with the maximum value intended to approximate the highest intensity stimulus provided in the behavioural experiments of Fig. 1. The first processing layer has two nodes, each representing one or more neurons: (1) a ‘pure’ node with output  $g_p(E_{\text{Mech}})$  that receives only mechanosensory input; and (2) a ‘mixed’ node with output  $g_m(E_{\text{Mech}}, E_{\text{Noci}})$  that receives input from both sensory modalities. The second processing layer is a single node with output  $g_B(g_p, g_m)$  that receives input from both nodes of the first processing layer. The output of the second layer constitutes the output of the circuit.

We considered the steady-state output of the network, assuming that the response of each node is a sigmoidal function of its total input, with a lower threshold below which output is near-zero and an upper saturation point. We modelled this as a logistic function<sup>78</sup>:

$$f(E; \theta, \beta) = C_{\theta, \beta} \frac{1}{1 + e^{-\frac{(E - \theta)}{\beta}}}$$

with total input  $E$ , threshold  $\theta$ , transition width  $\beta$ , and a constant  $C_{\theta, \beta}$  defined so that  $f(100) = 100$ . We set  $\beta = 10$  for all nodes, which makes the transition between

low and high output cover about half of the input range. We omit  $\beta$  in subsequent equations for brevity.

The output of the pure node in the first processing layer is given by:  $g_p(E_{\text{Mech}}) = f(E_{\text{Mech}}; \theta_p)$

For the mixed node, we take the total input to be a weighted sum of the sensory inputs:  $g_m(E_{\text{Mech}}, E_{\text{Noci}}) = f(w_M E_{\text{Mech}} + (1 - w_M) E_{\text{Noci}}; \theta_M)$  where  $0 \leq w_M \leq 1$  measures the relative weighting of mechanosensory input. To require that the maximum total input each node can receive is the same, the weights sum to one.

For the second layer, we take total input to be a weighted sum of the outputs from the nodes in the first layer:

$$g_B(E_{\text{Mech}}, E_{\text{Noci}}) = f(w_B g_p(E_{\text{Mech}}) + (1 - w_B) g_m(E_{\text{Mech}}, E_{\text{Noci}}); \theta_B)$$

where  $0 \leq w_B \leq 1$  measures the weighting of the pure chordotonal node in the first layer.

A common feature of multisensory circuits is their enhanced sensitivity to combinations of weak stimuli presented together. To consider this property in the context of our circuit, we looked for circuit responses that are maximally sensitive to multisensory stimuli, but that are also consistent with basic experimental observations. We treated this as a constrained optimization problem; we found mixing parameters  $w_M$  and  $w_B$  that optimize a measure of multisensory sensitivity, subject to the constraint that the responses to unimodal stimuli are similar to experimental observations (Extended Data Fig. 8b–d). We looked at the resulting solutions for a range of threshold parameters.

For the sensitivity measure, we assumed that the optimal solutions are responsive to combinations of both inputs (Extended Data Fig. 8b), as measured by the integrated response along a Gaussian-weighted band centred along the  $E_{\text{Mech}} = E_{\text{Noci}}$  diagonal line:

$$S(w_M, w_B) = \int_0^{100} \int_0^{100} g_B(E_{\text{Mech}}, E_{\text{Noci}}) e^{-(E_{\text{Mech}} - E_{\text{Noci}})^2 / 4d^2} dE_{\text{Mech}} dE_{\text{Noci}}$$

where  $d$  measures the width of the band, which we set to 20 (Extended Data Fig. 8c). Although this condition alone would encourage strong responses to extremely low values of input stimulus, an undesirable situation, the combination of the constraint and the monotonicity of the response functions ensure that this cannot occur.

For the constraint, we demanded that intense unimodal input match observations (see Fig. 1c): (1) that intense, pure chordotonal input induced no rolling; and (2) intense, pure MD IV input induced a modest, but non-zero, fraction of animals to roll (Extended Data Fig. 8d). We quantified this as:

$$h(w_M, w_B) =$$

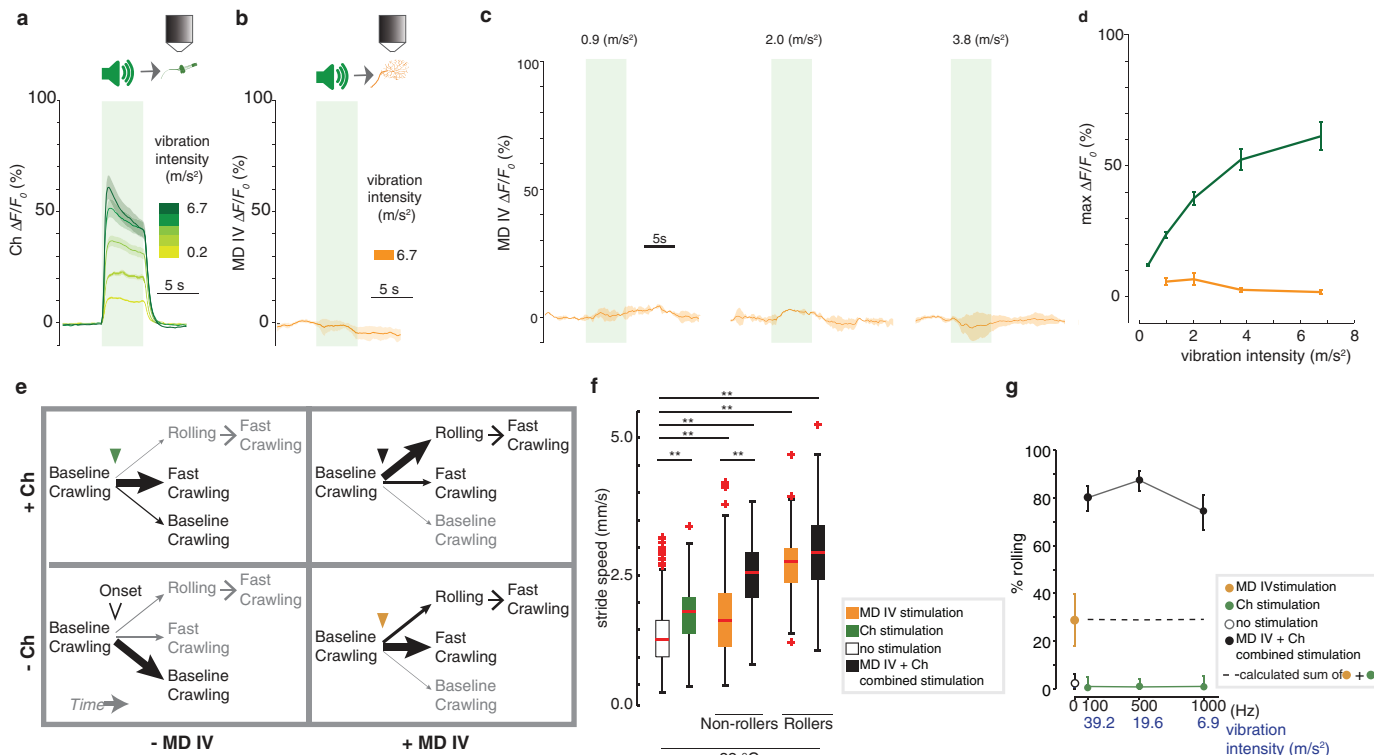
$$\sqrt{(g_B(0, 100; w_M, w_B) - a_{\text{Noci}})^2 + (g_B(100, 0; w_M, w_B) - a_{\text{Mech}})^2}$$

where we set  $a_{\text{Noci}} = 30$  and  $a_{\text{Mech}} = 0$  (Extended Data Fig. 8e).

We then calculated optimal connection weights given neuron thresholds. We assumed that the pure mechanosensory interneuron does not have an extremely high threshold, set  $\theta_p$  to a value between 30 and 50 and explored the constrained optimization problem for  $\theta_M$  and  $\theta_B$  values between 10 and 80. For each set of parameters, the multilevel convergence solution was defined as the circuit output corresponding to the parameters  $(w_M, w_B)$  that maximize  $S(w_M, w_B)$  subject to  $h(w_M, w_B) < h_0$ . We similarly defined the early convergence solution as the circuit with the  $w_M$  that maximizes  $S(w_M, 0)$  subject to  $h(w_M, 0) < h_0$ . We set  $h_0 = 3$  to ensure strong compliance with our unimodal constraints and numerically computed and compared solutions across a grid of  $w_B$  and  $w_B$  values starting at 0 with 0.01 spacing (Extended Data Fig. 8f). To check the robustness of early and multi-level convergence solutions to threshold parameters, we explored multiple values of  $\theta_B$  and  $\theta_B$  (Extended Data Fig. 8g).

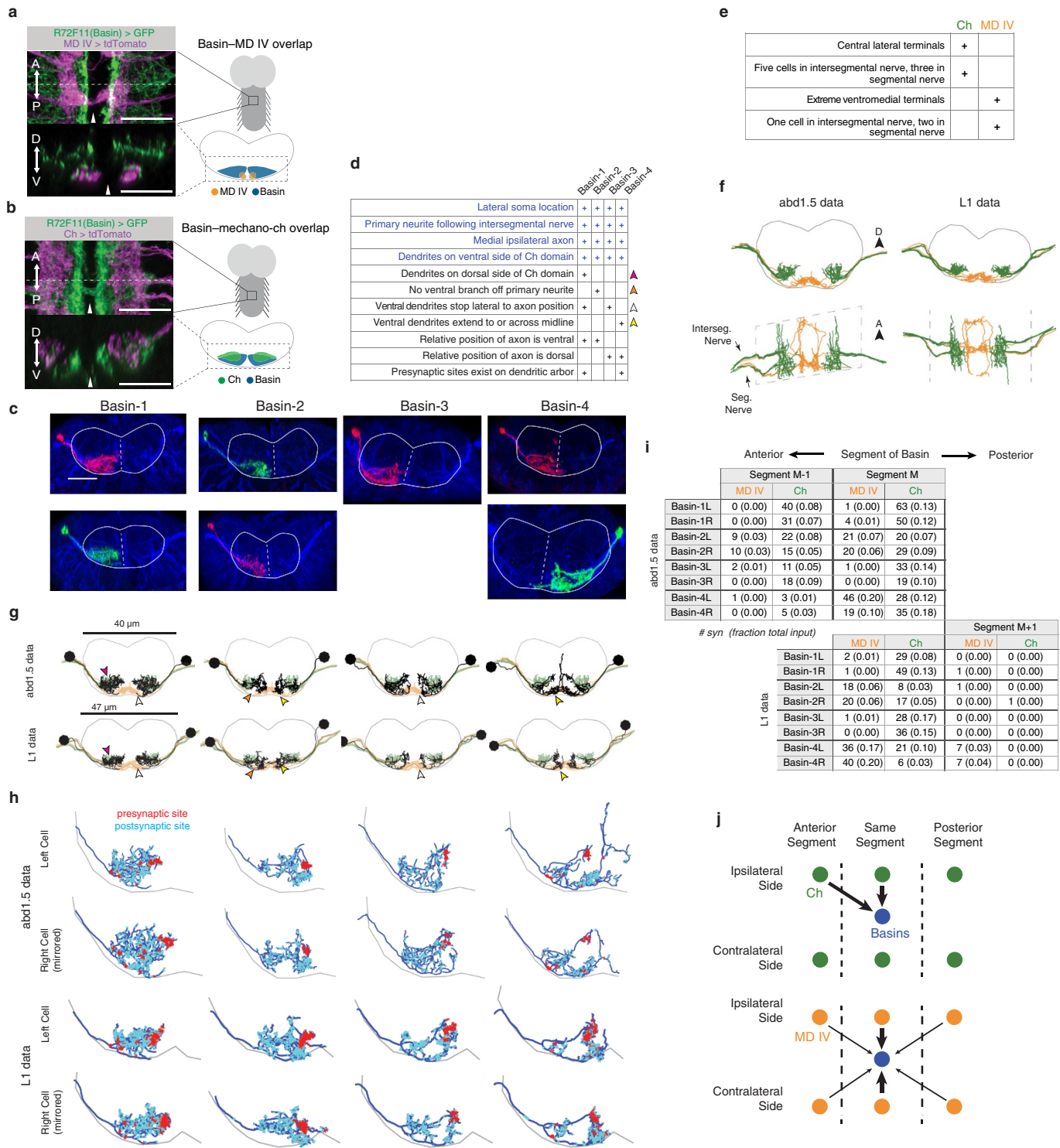
51. Jenett, A. et al. A GAL4-driver line resource for *Drosophila* neurobiology. *Cell Rep.* **2**, 991–1001 (2012).
52. Hamada, F. N. et al. An internal thermal sensor controlling temperature preference in *Drosophila*. *Nature* **454**, 217–220 (2008).
53. Kang, K. et al. Modulation of TRPA1 thermal sensitivity enables sensory discrimination in *Drosophila*. *Nature* **481**, 76–80 (2012).
54. Pfeiffer, B. D., Truman, J. W. & Rubin, G. M. Using translational enhancers to increase transgene expression in *Drosophila*. *Proc. Natl. Acad. Sci. USA* **109**, 6626–6631 (2012).
55. Chen, T.-W. et al. Ultrasensitive fluorescent proteins for imaging neuronal activity. *Nature* **499**, 295–300 (2013).
56. Tian, L. et al. Imaging neural activity in worms, flies and mice with improved GCaMP calcium indicators. *Nature Methods* **6**, 875–881 (2009).

57. Ainsley, J. A. *et al.* Enhanced locomotion caused by loss of the *Drosophila* DEG/ENaC protein Pick-pocket1. *Curr. Biol.* **13**, 1557–1563 (2003).
58. Baines, R. A., Uhler, J. P., Thompson, A., Sweeney, S. T. & Bate, M. Altered electrical properties in *Drosophila* neurons developing without synaptic transmission. *J. Neurosci.* **21**, 1523–1531 (2001).
59. Lima, S. Q. & Miesenbck, G. Remote control of behavior through genetically targeted photostimulation of neurons. *Cell* **121**, 141–152 (2005).
60. von Philipsborn, A. C. *et al.* Neuronal control of *Drosophila* courtship song. *Neuron* **69**, 509–522 (2011).
61. Calleja, M., Moreno, E., Pelaz, S. & Morata, G. Visualization of gene expression in living adult *Drosophila*. *Science* **274**, 252–255 (1996).
62. Luan, H., Peabody, N. C., Vinson, C. R. & White, B. H. Refined spatial manipulation of neuronal function by combinatorial restriction of transgene expression. *Neuron* **52**, 425–436 (2006).
63. Struhl, G. & Basler, K. Organizing activity of wingless protein in *Drosophila*. *Cell* **72**, 527–540 (1993).
64. Swierczek, N. A., Giles, A. C., Rankin, C. H. & Kerr, R. A. High-throughput behavioral analysis in *C. elegans*. *Nature Methods* **8**, 592–598 (2011).
65. Kabra, M., Robie, A. A., Rivera-Alba, M., Branson, S. & Branson, K. JAABA: interactive machine learning for automatic annotation of animal behavior. *Nature Methods* **10**, 64–67 (2013).
66. Schneider, C. A. *et al.* NIH Image to ImageJ: 25 years of image analysis. *Nature Methods* **9**, 671–675 (2012).
67. Verstreken, P., Ohyama, T. & Bellen, H. J. in *Exocytosis and Endocytosis* 349–369 (Springer, 2008).
68. Glasbey, C. A. An analysis of histogram-based thresholding algorithms. *CVGIP. Graph. Models Image Proc.* **55**, 532–537 (1993).
69. Sato, T. A modified method for lead staining of thin sections. *J. Electron Microsc. (Tokyo)* **17**, 158–159 (1968).
70. Suloway, C. *et al.* Automated molecular microscopy: the new Leginon system. *J. Struct. Biol.* **151**, 41–60 (2005).
71. Saalfeld, S., Cardona, A., Hartenstein, V. & Tomancak, P. CATMAID: collaborative annotation toolkit for massive amounts of image data. *Bioinformatics* **25**, 1984–1986 (2009).
72. Prokop, A. & Meinertzhagen, I. A. Development and structure of synaptic contacts in *Drosophila*. *Semin. Cell Dev. Biol.* **17**, 20–30 (2006).
73. Landgraf, M., Snchez Soriano, N., Technau, G. M., Urban, J. & Prokop, A. Charting the *Drosophila* neuropile: a strategy for the standardised characterisation of genetically amenable neurites. *Dev. Biol.* **260**, 207–225 (2003).
74. Grueber, W. B., Jan, L. & Jan, Y. Tiling of the *Drosophila* epidermis by multidendritic sensory neurons. *Development* **129**, 2867–2878 (2002).
75. Bastian, M. *et al.* Gephi: an open source software for exploring and manipulating networks (International AAAI Conference on Weblogs and Social Media, 2009).
76. Bate, M., Goodman, C. & Spitzer, N. Embryonic development of identified neurons: Segment-specific differences in the H cell homologues. *J. Neurosci.* **1**, 103–106 (1981).
77. Jefferis, G. S. *et al.* Comprehensive maps of *Drosophila* higher olfactory centers: spatially segregated fruit and pheromone representation. *Cell* **128**, 1187–1203 (2007).
78. Dayan, P. & Abbott, L. F. *Theoretical Neuroscience* (MIT Press, 2001).



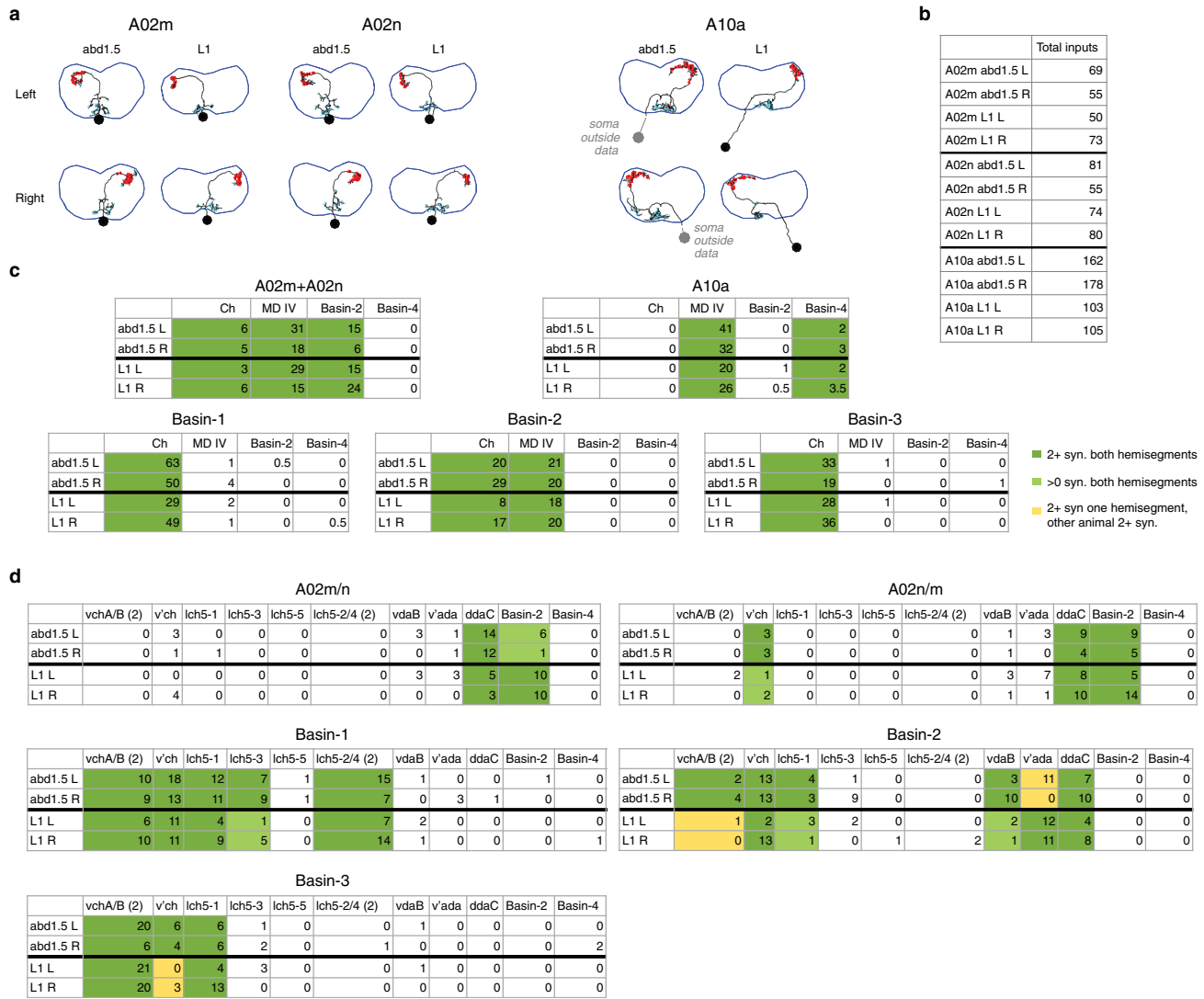
**Extended Data Figure 1 | This figure relates to Fig. 1a–d.** Chordotonal (Ch) neurons respond to vibration in a ‘dose-dependent’ manner, but MD IV neurons do not, consistent with previous reports. **a**, 1,000 Hz vibration evokes calcium transients (mean  $\pm$  s.e.m. in this and all subsequent figures) in chordotonal (*ch-GAL4>UAS-GCaMP6s*), in a dose-dependent manner. **b**, **c**, Calcium transients of MD IV neurons in response to different vibration (1,000 Hz) intensities reveal no response to vibration (*MD IV-GAL4>UAS-GCaMP6s*). **d**, Quantification of calcium transients in mechanosensory (black) and nociceptive (orange) neurons from (a–c).  $n = 3$  trials in each condition. **e**, A schematic of larval reactions to unimodal and multimodal stimuli. Line thickness qualitatively reflects the probability of the behaviour transition occurring in the absence of stimulation (bottom left) and after the onset of MD IV activation (orange triangle, bottom right), vibration (green triangle, top left), or their combination (black triangle, top right). Behaviours in grey occur with extremely low frequency. In response to nociceptive or combined stimulation animals can select one of two types of escapes responses: (1) roll-fast crawl; or (2) fast crawl alone. Even in response to combined stimulation the selection is probabilistic; the majority of animals select roll-fast crawl, but some select fast crawl without rolling. **f**, Crawling stride speed in the absence of stimulation (white) and following 1,000 Hz, 6.7 m s<sup>-2</sup> vibration (green) (in *MD IV-GAL4>+* larvae); thermogenetic nociceptive activation (32 °C, in *MD IV-GAL4>UAS-dTRPA1* larvae) (orange); or their combination (grey). In the nociceptive and combined condition, we separately analysed the stride speed of animals that did not roll (non-rollers) and those that rolled (rollers) following stimulation. As previously described, vibration alone evoked an increase in stride speed. Nociceptive activation alone, or in combination with vibration, also evoked an increase in stride speed, both in animals that did not roll and in animals that did roll, after rolling. Combining vibration with nociceptive stimulation in animals that selected fast crawl significantly increased stride speed compared to either stimulation alone. Vibration combined with nociceptive stimulation therefore affects both aspects of the escapes response, facilitating the triggering of rolling (Fig. 1e, f) and increasing crawling stride speed in animals that do not roll. Wilcoxon rank sum test with Holm-Bonferroni correction. \*\* $P < 0.0001$ . **g**, The synergistic effect on rolling of combining vibration with nociceptive stimulation is observed across a range of frequencies. Rolling probabilities of *MD IV-GAL4>UAS-dTrpA1* (nociceptive and combined conditions) or *MD IV-GAL4>+* (no stimuli and mechanosensory conditions) animals during vibration stimulation at different frequencies, either alone (green) or in combination with thermogenetic activation of nociceptive neurons (32 °C) (grey). See Supplementary Table 3 for  $n$  (animals) in this and all other Extended Data Figures. See Supplementary Table 2 for a list of genotypes used all Figures.

*GAL4>UAS-dTRPA1* larvae) (orange); or their combination (grey). In the nociceptive and combined condition, we separately analysed the stride speed of animals that did not roll (non-rollers) and those that rolled (rollers) following stimulation. As previously described, vibration alone evoked an increase in stride speed. Nociceptive activation alone, or in combination with vibration, also evoked an increase in stride speed, both in animals that did not roll and in animals that did roll, after rolling. Combining vibration with nociceptive stimulation in animals that selected fast crawl significantly increased stride speed compared to either stimulation alone. Vibration combined with nociceptive stimulation therefore affects both aspects of the escapes response, facilitating the triggering of rolling (Fig. 1e, f) and increasing crawling stride speed in animals that do not roll. Wilcoxon rank sum test with Holm-Bonferroni correction. \*\* $P < 0.0001$ . **g**, The synergistic effect on rolling of combining vibration with nociceptive stimulation is observed across a range of frequencies. Rolling probabilities of *MD IV-GAL4>UAS-dTrpA1* (nociceptive and combined conditions) or *MD IV-GAL4>+* (no stimuli and mechanosensory conditions) animals during vibration stimulation at different frequencies, either alone (green) or in combination with thermogenetic activation of nociceptive neurons (32 °C) (grey). See Supplementary Table 3 for  $n$  (animals) in this and all other Extended Data Figures. See Supplementary Table 2 for a list of genotypes used all Figures.



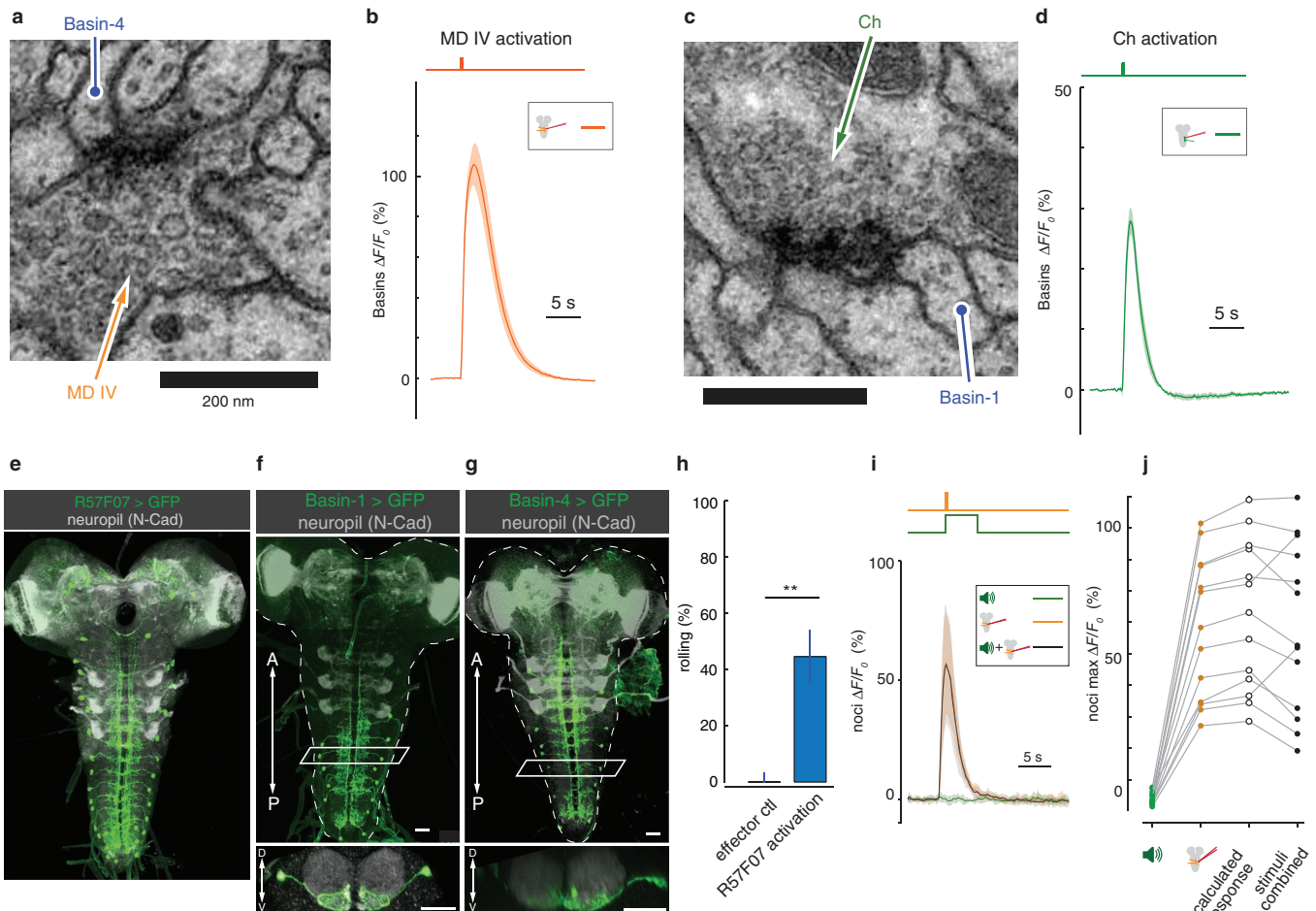
**Extended Data Figure 2 | This figure relates to Fig. 2a, b, a, b,** Confocal images of basins (green) and nociceptors (**a**) or chordotonal (**b**) (both in magenta), with cartoons to demonstrate their position within the nerve cord. **c**, Confocal images of individual Basins (in addition to those shown in Fig. 3a) visualized with a FLP-based method. Outline, neuropil boundary. Scale bar, 30  $\mu\text{m}$ . **d**, Table of morphological features based on which Basins are uniquely distinguishable from other interneurons (blue) and individual Basin types from each other (purple). **e**, The table of morphological features based on which the mechanosensory chordotonal (Ch; green) and the nociceptive (orange) neuron projections are uniquely identifiable. **f**, Electron microscopy reconstructions of MD IV (orange) and chordotonal (green) axons in two abdominal segments, from two different animals. Top, reconstructions from the A3 segment in the smaller electron microscopy volume (comprising 1.5 abdominal segments: A3 and a part of A2) shown in Fig. 2. Bottom, reconstructions from the segment A1 in the comprehensive electron microscopy volume that spans the entire nervous system (L1 electron microscopy volume, see Fig. 5 and Supplementary Video 7). Outlines indicate approximate neuropil boundaries. Scale bar, 20  $\mu\text{m}$ . **g**, Electron microscopy reconstructions of nociceptive (orange) and mechanosensory (green) axons and of the four Basin types (black) in the two abdominal segments, from two different animals. Top, A3 segment from the smaller 1.5 abdominal segment volume. Bottom, A1 segment in the comprehensive L1 electron microscopy volume. Outlines indicate

approximate neuropil boundaries. Scale bar, 20  $\mu\text{m}$ . The MD IV and chordotonal terminals span the ventromedial and ventrocentral nerve cord domains, respectively. Basin-2 and Basin-4 dendrites overlap with chordotonal and MD IV terminals. **h**, Detailed views of the neuronal arbors and synaptic locations of each Basin cell type from the two segments (from the two animals). Cells on the right side are mirrored for easier comparison. The location of synaptic domains is conserved across hemisegmental homologues and animals. The dendritic arbors of individual Basins across all four hemisegments are highly stereotyped and uniquely recognizable. **i**, Tables show the numbers of synapses that Basins in the A3 segment (from the smaller 1.5 segment electron microscopy dataset, top) and in the A1 segment (from the comprehensive L1 electron microscopy volume, bottom) receive from MD IV and chordotonal neurons in their own and in adjacent abdominal segments. See also Supplementary Tables 4a and 5a for more information. Both the left and right Basin-1 and Basin-3 homologues reproducibly received many synapses (each >25 synapses and >15% of total input, on average) from chordotonal in both animals, but very few (no more than 1% of total input synapses) from MD IV neurons. Both the left and right Basin-2 and Basin-4 homologues received many inputs from both chordotonal (on average >20 synapses and >10% total input) and MD IV (on average >20 synapses and >10% total input) neurons. **j**, Schematic representation of the distribution of inputs from MD IV and chordotonal from adjacent segments onto Basins.



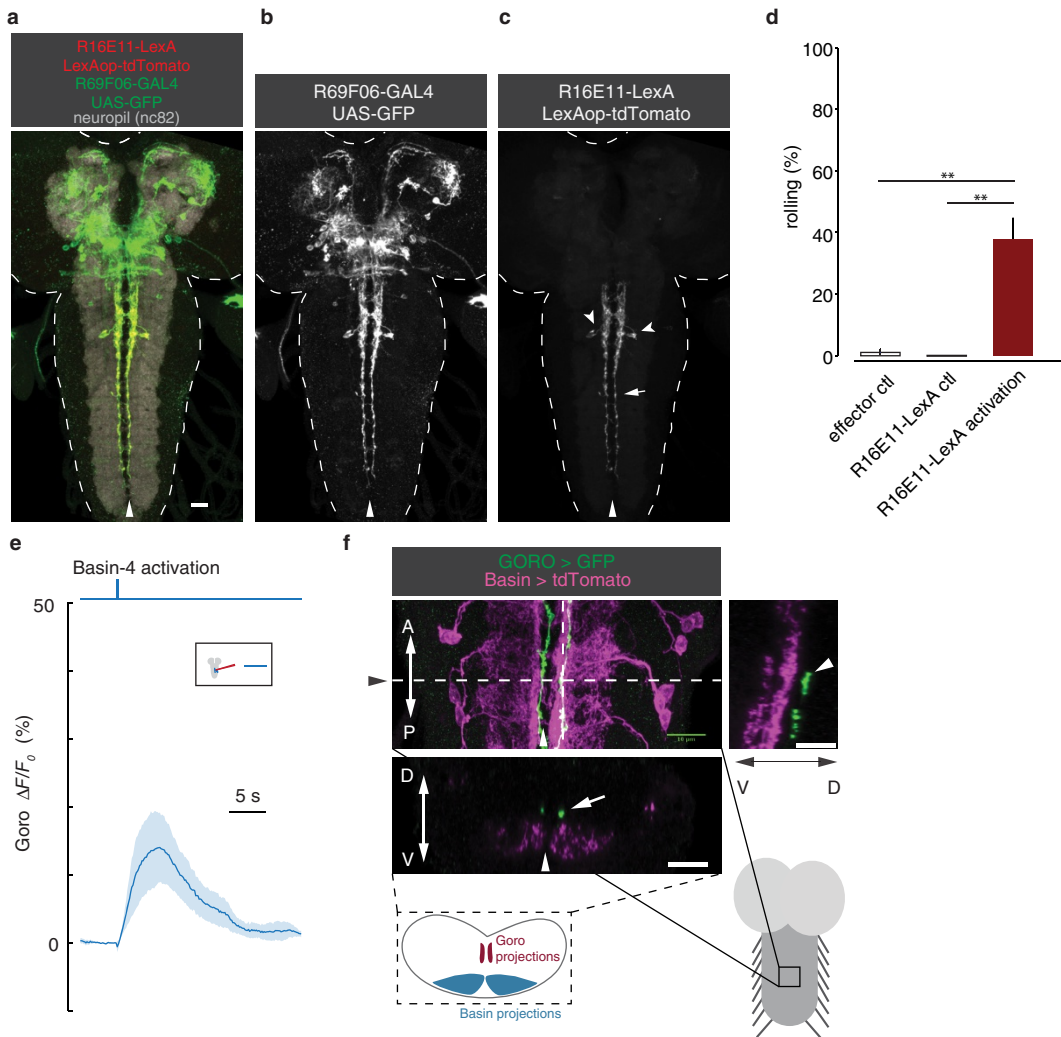
**Extended Data Figure 3 | Reproducibility of the wiring diagram across animals.** **a**, Electron microscopy reconstructions of the local interneurons downstream of both the MD IV and Basin neurons in both electron microscopy volumes; the volume comprising 1.5 abdominal (A2/A3) nerve cord segments of one animal (abd1.5, Fig. 2e), and the electron microscopy volume comprising the entire nervous system of another (L1, Fig. 5a and Supplementary Video 7). These local neurons (as well as the Basins shown in Fig. 2f and Extended Data Fig. 2h) with cell bodies and the majority of their arbor in the same segment as the sensory neurons are readily identifiable in both volumes and can be used to assess the reproducibility of sensory–interneuron and interneuron–interneuron connectivity across animals. Three distinct short-range interneuron types (A02m, A02n and A10a) received at least two synapses from nociceptive sensory neurons in both animals. A02m/n and A02n neurons also received inputs from Basin-2 or Basin-4 (Supplementary Information (Supplementary Atlas section)). The two interneurons A02m and A02n belong to the same lineage (lineage 2), have indistinguishable projections and connectivity, and can only be distinguished based on a small difference in the dorsoventral cell body location. In contrast, Basin-1, Basin-2, Basin-3 and Basin-4, even though they belong to the same lineage (lineage 9), all have distinct projections (and connectivity) and can each be considered a unique

neuron type. A10a also have unique projections and belong to lineage 10. **b**, Total number of inputs each neuron in **a** receives. **c**, Reproducibility of connections between neuron types across individuals. Table shows class level connectivity between neurons in the abd1.5 and L1 data sets. Values given are the total sum of all synapses for all members of each class. 100% of connections with at least two synapses between homologous neuron types that were reproducible across the same individual were also reproducible across individuals; that is, the connection between those neurons existed in the other individual. **d**, Reproducibility of connections between individual neurons across individuals. Table shows connectivity between individual neurons in the abd1.5 and L1 data sets. Whenever two or more synapses were found between homologous neurons in both hemisegments in one animal, either two or more were also found in both hemisegments in the other animal (dark green cells); or at least one synapse per edge was found in both hemisegments in the other animal (light green cells); or two or more synapses were found in at least one hemisegment of the other animal (yellow cells). Thus, in 100% of cases in which a connection was present between homologues on both sides in one individual it was also present between homologues in the other individual, at least on one side.



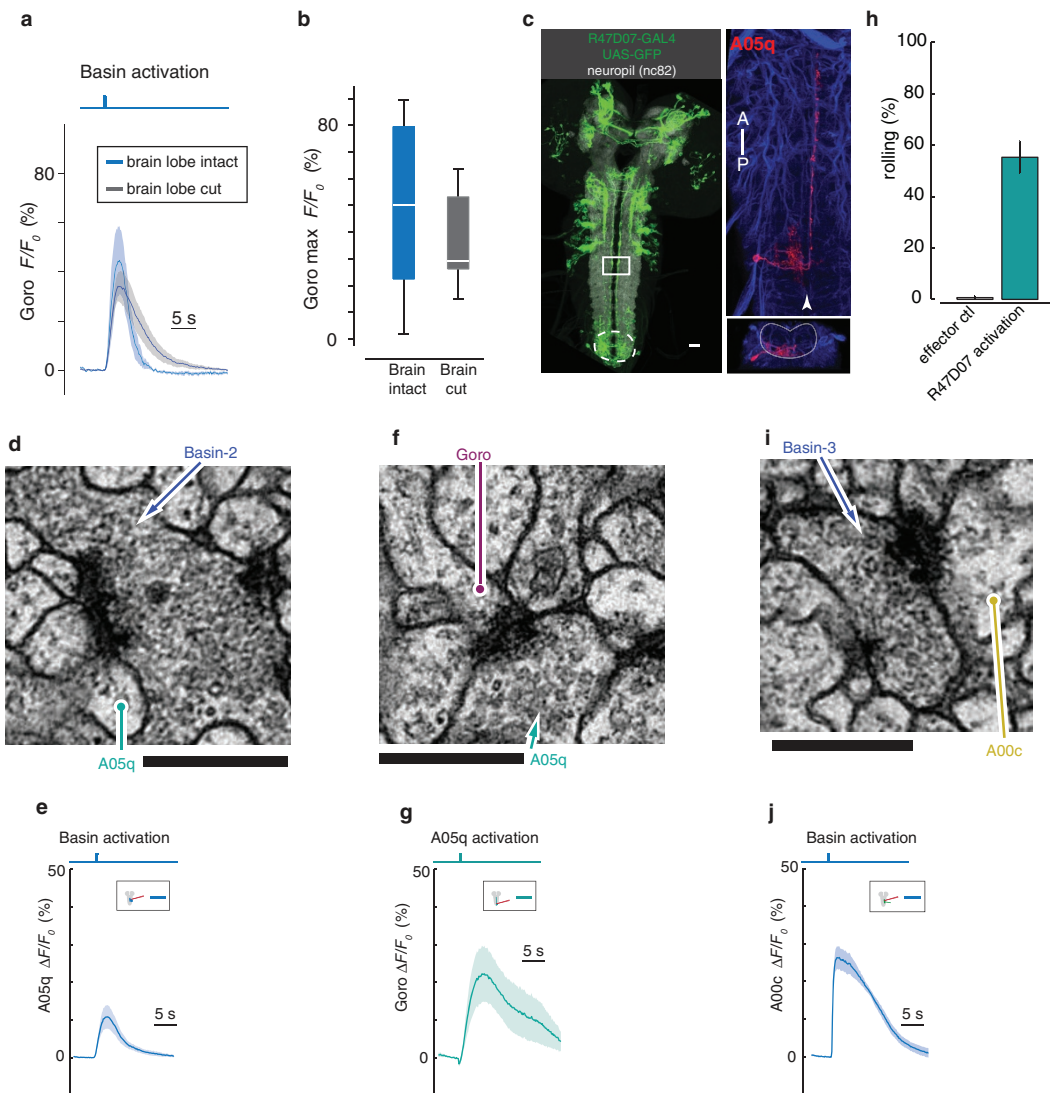
**Extended Data Figure 4 | This figure relates to Figs 2 and 3.** a, c, Electron micrographs of representative synapses formed by MD IV and chordotonal (Ch) projections onto Basins containing a T-bar ribbon. Circles point to the postsynaptic neuron and arrows point to vesicle clouds in the presynaptic terminals. All synapses have small clear-core vesicles associated with fast chemical neurotransmitters such as acetylcholine, glutamate, or GABA. Scale bars are 200 nm. b, d, Calcium transients evoked in Basins by MD IV (b) and chordotonal (d) activation by local ATP injection. The ATP-gated channel, P2X<sub>2</sub>, is expressed in MD IV (b) and chordotonal (d) neurons and GCaMP6 is expressed in Basins (in *MD IV-lexA>lexAop-P2X<sub>2</sub>; R72F11-GAL4>UAS-GCaMP6* (b) and *Ch-lexA>lexAop-P2X<sub>2</sub>; R72F11-GAL4>UAS-GCaMP6* (d) animals). n = 30 trials (b), and 18 trials (d). Functional connectivity experiments suggest the connection from sensory neurons onto Basins is excitatory. Since chordotonal neurons are the only neurons that respond to vibration<sup>32,35</sup> we used vibration in subsequent experiments so that we could activate chordotonal with vibration, and MD IV with P2X<sub>2</sub> and ATP injection,

in the same animal. e, R57F07 drives expression in Basin-4 neurons and in a few brain neurons. R57F07 was therefore used for generating the Basin-4 selective split-GAL4 line shown in g. g, h, Expression patterns of driver lines selective for Basin-1 (*R20B01*) and Basin-4 (*R72F11* and *R57F07* intersection) neurons (green). Scale bar, 25  $\mu$ m. f, Activation of *R57F07* is sufficient to evoke rolling in 45% of animals. Intersecting the parent line *R57F07* with *R72F11* (both drive expression in Basin-4 neurons and evoke rolling) results in a split-GAL4 line that drives expression selectively in Basin-4 neurons, shown in g. i, j, Negative control for Fig. 4d, f. i, Calcium transients in MD IV terminals observed in response to vibration (1,000 Hz, 6.8 m s<sup>-2</sup>), MD IV activation by local ATP injection or their combination (in *MD IV-lexA>lexAop-P2X<sub>2</sub>; MD IV-GAL4>UAS-GCaMP6* animals). n = 14 trials. j, Maximum  $\Delta F/F_0$  of calcium transients in response to mechanosensory, nociceptive, and combined simulation from i. Unlike Basin-4 (Fig. 3b, c), the MD IV neurons do not respond more to the combination of stimuli compared to MD IV activation alone.



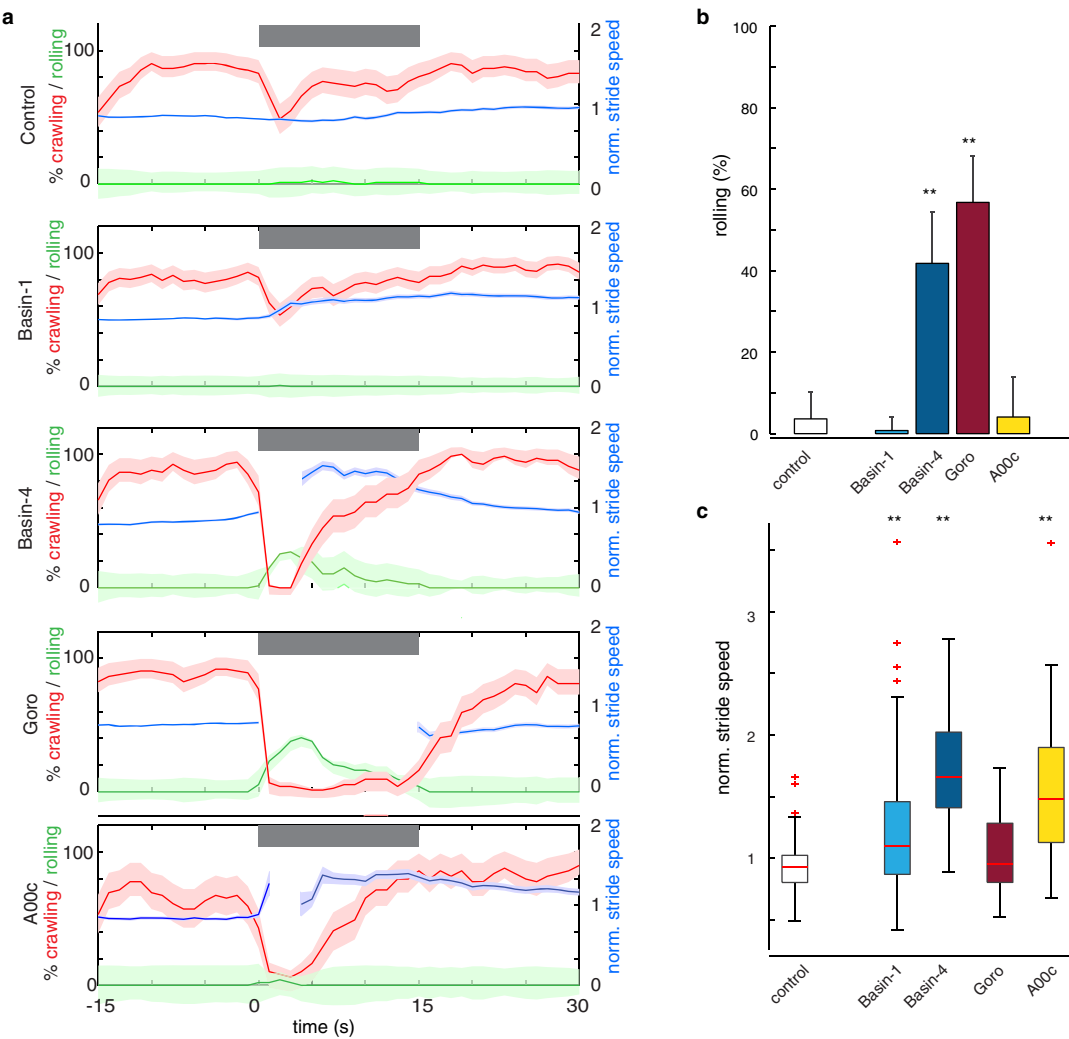
**Extended Data Figure 5 | This figure relates to Fig. 4. a–c.** The *R16E11-LexA* line faintly, but selectively, drives expression in the same pair of thoracic neurons (Goro neurons) as the *R69F06 GAL4* line. **a**, Co-localization of *R16E11-LexA* and *R69F06-GAL4* expression in the same nervous system (genotype: *R16E11-lexA/LexAop-mry-tdTomato; R69F06-GAL4, UAS-mry-GFP*). *R16E11-lexA>lexAop-tdTomato* (red) and *R69F06-GAL4>UAS-GFP* (green) co-localize in the two Goro cell bodies and their projections in the nerve cord (yellow). **b, c**, Single-channel images from **a**. Scale bar, 20  $\mu$ m. **d**, Thermogenetic activation (32 °C) of the single pair of Goro neurons using the *R16E11* line (*R16E11-lexA>lexop-dTRPA1*) evoked rolling in 36% of animals. Activating neurons in *R69F06* evokes even more rolling (86%, Fig. 4a). *R69F06* drives expression in Goro neurons more strongly than *R16E11*, but it

also drives expression in more neurons. Using a FLP-based intersection between *R16E11-lexA* and *R69F06* (see Methods), we found that 76% of animals with expression of dTRPA1 selectively in Goro rolled when exposed to restrictive temperature (32 °C). Thus, activating the single pair of command-like Goro neurons evokes rolling. **e**, Calcium transients in Goro dendrites in response to selective Basin-4 activation by local ATP injection ( $n = 12$  trials). The ATP-gated P2X<sub>2</sub> channel and GCaMP6 are expressed selectively in Basin-4 and Goro neurons, respectively (in *Basin-4-Gal4>UAS-P2X<sub>2</sub>; Goro-lexA(R69F06-lexA)>lexAop-GCaMP6* animals). **f**, Basin (magenta) and Goro (green) projections do not co-localize (in *16E11-lexA>LexAop-tdTomato; R72F11-GAL4>UAS-GFP* larvae), indicating that the two cell types that are functionally connected cannot be directly synaptically connected.



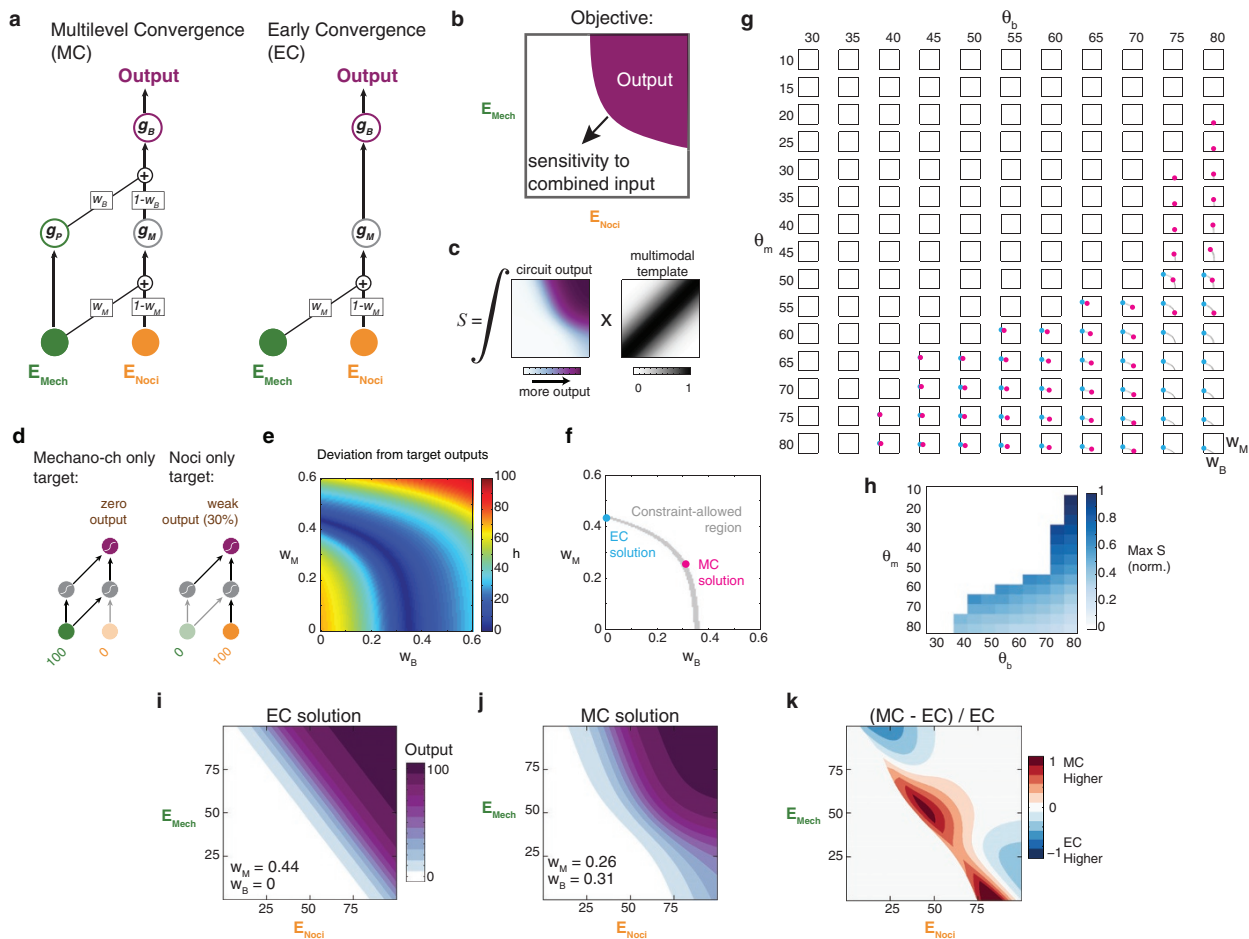
**Extended Data Figure 6 | This figure relates to Fig. 5.** **a**, The nerve cord Basin–Goro pathway is sufficient to activate the Goro neurons. Calcium transients in Goro dendrites evoked by Basin activation by local ATP injection with the brain lobes intact ( $n = 15$  trials) or removed ( $n = 24$  trials) (in *R72F11-LexA>LexAop-P2X<sub>2</sub>; Goro-GAL4(R69F06)>GCaMP6* animals). **b**, Quantification of **a**. The difference is not significant. Error bars show s.e.m. **c**, Left, *R47D07* drives expression in A05q neurons (that receive direct inputs from Basin-2 and synapse onto Goro neurons) and in other neurons in thorax and brain (green, visualized with anti-GFP). In abdominal segments A8 and A7, the only neurons labelled with this line are the A05q neurons (dashed circle). The rest of the nervous system (grey) is visualized with anti-N-cadherin. White square, A05q axon terminals that synapse onto Goro dendrites. Scale bar, 25  $\mu$ m. Note that this line also drives expression in developing adult neurons in thorax and brain that are not functional in the larval nervous system (secondary lineages). Right, image of individual A05q cells (magenta) visualized with a FLP-based strategy in *R47D07*, in top-down (top) and cross-section (bottom) views. Arrowheads indicate midline. Thin white lines indicate neuropil boundary. **d**, **f**, **i**, Electron micrographs of representative synapses formed by

Basin-2 onto A05q (**d**), A05q onto Goro (**f**) and Basins onto A00c (**i**) containing T-bar ribbons. Circles point to the postsynaptic neuron and arrows point to vesicle clouds in the presynaptic terminals. All synapses have small clear-core vesicles associated with fast chemical neurotransmitters such as acetylcholine, glutamate, or GABA. Scale bars, 200 nm. **e**, Calcium transients in A05q axon terminals (square in **c**) evoked by Basin activation using local ATP injection (*R72F11-LexA>lexop-P2X<sub>2</sub>; R47D07-GAL4>UAS-GCaMP6*,  $n = 18$  trials) suggest a functionally excitatory connection. **g**, Calcium transients in Goro neurons evoked by A05q activation using local ATP injection specifically in the vicinity of A05q dendrites in A8 (dotted circle in **c**; *R47D07-GAL4>UAS-P2X<sub>2</sub>; Goro(R69E06-LexA>lexop-GCaMP6*,  $n = 18$  trials) suggest a functionally excitatory connection. **h**, Thermogenetic activation of neurons in *R47D07* triggers rolling (exposing *R47D07-GAL4>UAS-dTrpA1* animals to 32 °C). Control, +>UAS-dTrpA1. **j**, Calcium transients in A00c evoked by Basin activation using local ATP injection (*R72F11-LexA>lexop-P2X<sub>2</sub>; R71A10-GAL4>UAS-GCaMP6*,  $n = 15$  trials) suggest a functionally excitatory connection.



**Extended Data Figure 7 | Distinct neurons differentially control distinct aspects of the escape sequence.** **a**, Graphs show the time course of rolling (green) and crawling (red and blue) behaviours before, during and after a 15 sec (indicated by the grey box) optogenetic (617 nm red light) activation period. The percentage of larvae that are rolling (green line) or crawling (red line) at each time point is shown. The normalized speed of crawling strides (normalized by speed prior to optogenetic stimulation) is also shown for those animals that are crawling at the time (blue line). Means (dark line) and s.e.m. (shaded areas) are shown. Data are from  $+>UAS\text{-}CsChrimson$ ,  $basin1\text{-}GAL4>UAS\text{-}CsChrimson$ ,  $basin4\text{-}GAL4>UAS\text{-}CsChrimson$ ,  $Goro\text{-}GAL4(R69F06)>UAS\text{-}CsChrimson$ , or  $A00c\text{-}GAL4(R71A10)>UAS\text{-}CsChrimson$  animals, from top to bottom. **b**, Percentage of larvae that rolled at least once during the entire 15 sec activation window. Error bars are 95% confidence intervals. \*\* $P < 0.0001$ . Optogenetic activation of Basin-4 and Goro neurons evokes rolling, consistent with the results of thermogenetic activation experiments shown in Figs 2a, g and 4e. Note that the instantaneous percentage of rolling shown in **a** is always lower than the percentage shown in **b** because not all larvae roll at exactly the same time. **c**, Comparison of the normalized speed of crawling strides in response to

optogenetic activation. Boxes show medians (red) with 25th and 75th quantiles of the data. Whisker is 1.5 interquartile range (IQR) for the length of the whiskers. Red plus is outlier. \*\* $P < 0.0001$ . We observe that in control larvae, red light alone evoked a mild reduction in crawling speed, whereas Basin-1 activation evoked a mild, but significant, increase in stride speed and did not evoke rolling. Basin-4 activation evoked the entire escape sequence (roll followed by fast crawl). Note first an increase in instantaneous percentage of rolling larvae (peak in green line in **a**), followed by an increase in the instantaneous percentage of crawling larvae, and an increase in stride speed relative to the period prior to stimulation (peak in blue line in **a**). Goro neuron activation only evoked rolling and not crawling (note the percentage of crawling larvae is almost 0 during the optogenetic activation period). Furthermore there was no increase in relative stride speed following stimulation offset. Activation of the three A00c neurons with R71A10 was not sufficient to evoke rolling, but it was sufficient to evoke a mild, but significant, increase in stride speed. Thus, distinct neurons downstream of Basins appear to differentially control distinct aspects of the ‘roll-fast crawl’ escape sequence.



**Extended Data Figure 8 | Multilevel convergence can enhance sensitivity to weak multimodal stimuli.** A benefit of the multilevel architecture could be to amplify the effect of mechanosensory cues on nociceptive cues, increasing the sensitivity to relatively weak bimodal cues. To explore this idea further, we used a simple model to ask whether a two-level network with two levels of convergence (multilevel convergence; MC) can be more sensitive to relatively weak bimodal events than a network with only early convergence (EC). **a**, Schematic for a simple model of early and multilevel convergence networks (see Methods for details). We considered an early convergence and a multilevel convergence two-layer feed-forward circuit with two inputs, corresponding to MD IV ( $E_{Noci}$ ) and chordotonal ( $E_{Mech}$ ), and one output corresponding to rolling occurrence. We modelled steady-state firing rates, where the output of each model neuron is a sigmoidal logistic function (with a lower threshold and upper saturation) of a weighted sum of its inputs. One pathway remains only chordotonal, while the other mixes modalities only early, or at both levels, depending on weights ( $w_M$  and  $w_B$ ). **b–d**, Solutions for  $w_M$  and  $w_B$  are found using a constrained optimization procedure that maximizes sensitivity to weak bimodal inputs (**c**) within two experimentally observed unimodal target outputs (**d**): (1) that mechanosensory stimulus alone never evokes rolling; and (2) that the strongest MD IV stimulus alone evokes only 30% output (Fig. 1e, f and see Methods for details). **e**, Example deviation  $h$  from target outputs (see Methods) for multiple values of  $w_M$  and  $w_B$  for one set of thresholds ( $\theta_p = 40$ ;  $\theta_M = 50$ ;  $\theta_B = 75$ ). **f**, Values of  $w_M$  and  $w_B$  that maximize sensitivity  $S$  (dots) while also satisfying  $h < 3$  (grey area). **g**, Early and multilevel solutions (if they exist) for other thresholds. Solutions exist if one or both  $\theta_M$  or  $\theta_B$  is high

(keeping  $\theta_p = 40$ ). Note that although the optimal sensitivity multilevel convergence solution could have  $w_M = 0$  and thus effectively be an early convergence solution, this does not occur; multilevel convergence solutions are always more sensitive when they exist. Multilevel convergence solutions with  $w_B = 0$  are not shown since they do not exhibit multilevel convergence.

**h**, Sensitivity of the optimal multilevel convergence solution as a function of the same thresholds as in Extended Data Fig. 8g, normalized by the most sensitive multilevel convergence solution found. Multilevel convergence solutions are more sensitive to relatively weak multimodal stimuli than early convergence solutions. Across all thresholds tested, the most sensitive circuits occur for  $\theta_M = 50$  and  $\theta_B = 75$  (Extended Data Fig. 8k). For such parameters, no early convergence solutions satisfy the unimodal constraints, hence multilevel convergence solutions are overall the most sensitive. **i, j**, Example early convergence and multilevel convergence solutions for  $w_B$  and  $w_B$  that satisfy the condition in **d** for one set of neuronal firing thresholds ( $\theta_p = 40$ ;  $\theta_M = 50$ ;  $\theta_B = 75$ ). **k**, Subtracting the output of early convergence from the multilevel convergence circuit. The multilevel convergence circuit triggers more rolling than the early convergence circuit in response to relatively weak bimodal cues and strong unimodal MD IV cues, but less rolling than the early convergence circuit to strong unimodal chordotonal cues (top left corner). The multilevel convergence circuit thus offers a more complex response function with greater sensitivity and selectivity for multimodal and strong unimodal MD IV cues, but not chordotonal cues, and could enable enhanced selection of rolling to more threatening events and reduced selection of rolling to less threatening events.